# Figure 2

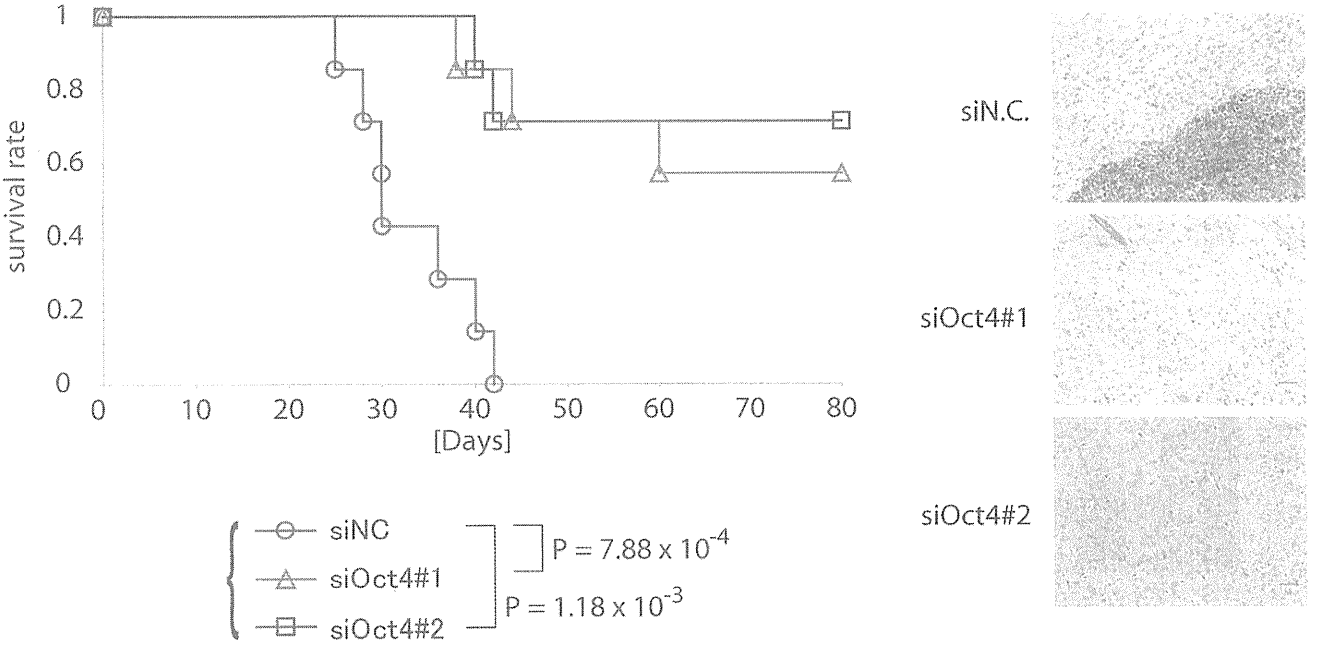

# Figure 3

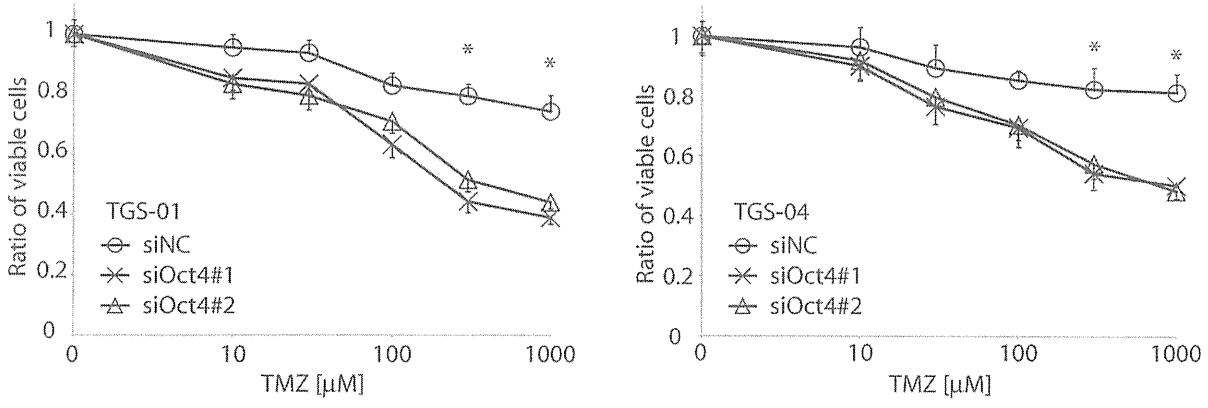

# Figure 4

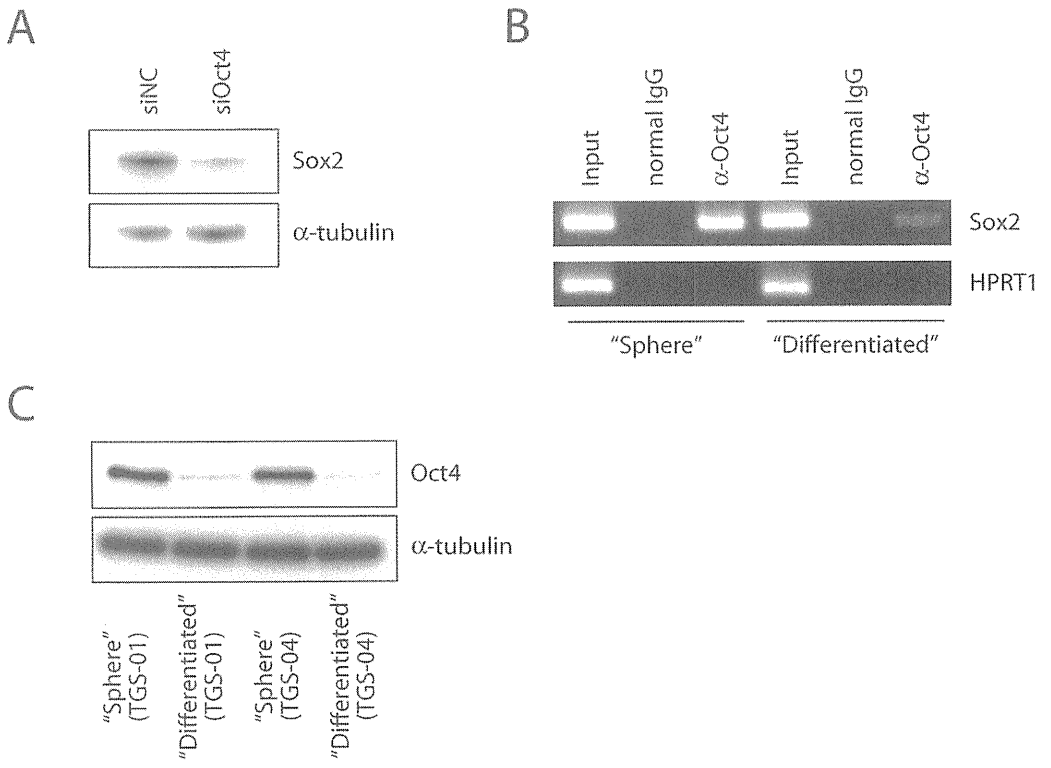

# Figure 5

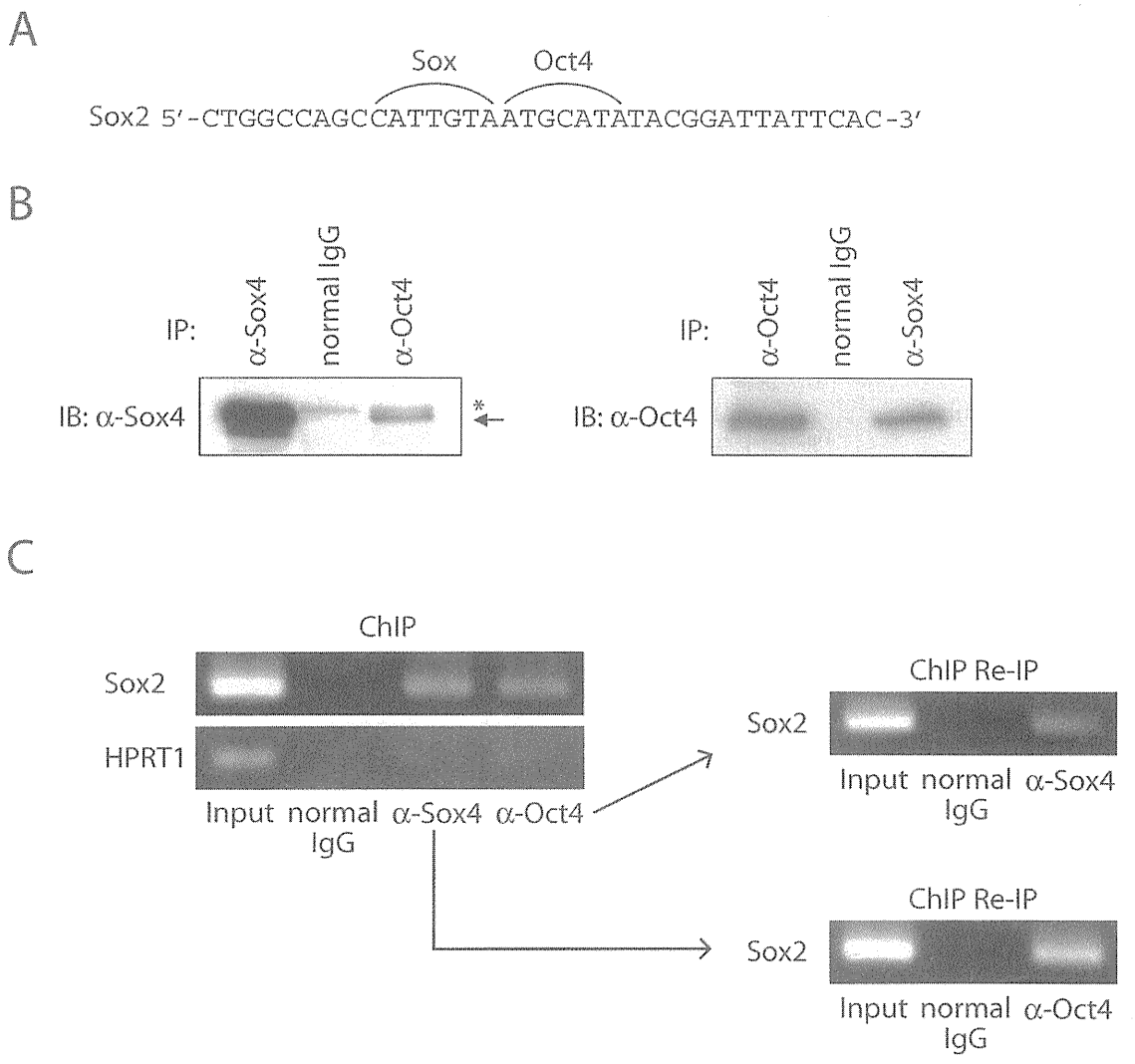

# Figure 6

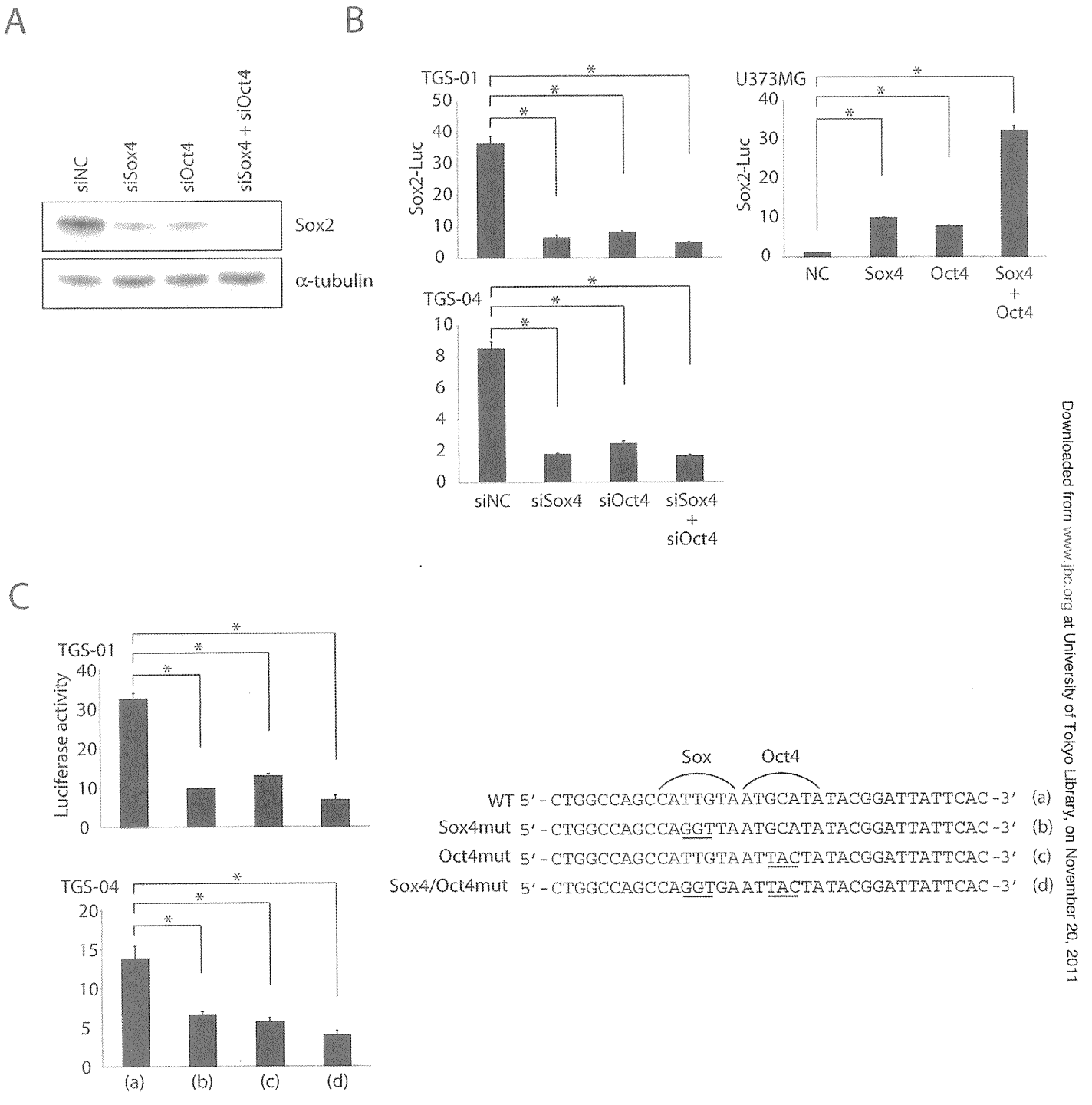

# Figure 7

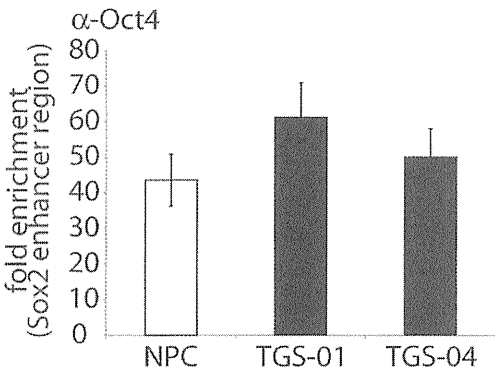


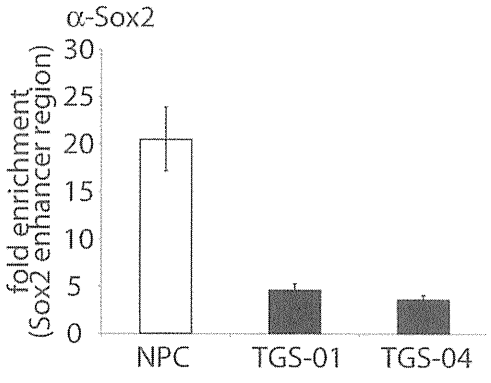


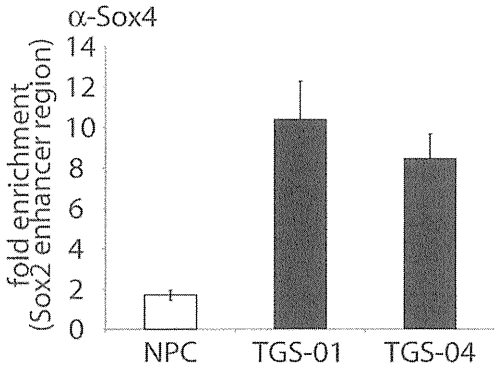

## References


Abrahamsen, A.F., Borge, L. & Holte, H. (1990) Infection after splenectomy for Hodgkin's disease. *Acta Oncologica*, **29**, 167–170.

Aleman, B.M., van den Belt-Dusebout, A.W., De Bruin, M.L., van 't Veer, M.B., Baaijens, M.H., de Boer, J.P., Hart, A.A., Klokman, W.J., Kuenen, M.A., Ouwens, G.M., Bartelink, H. & van Leeuwen, F.E. (2007) Late cardiotoxicity after treatment for Hodgkin lymphoma. *Blood*, **109**, 1878–1886.

Andersson, A., Naslund, U., Tavelin, B., Enblad, G., Gustavsson, A. & Malmer, B. (2009) Long-term risk of cardiovascular disease in Hodgkin lymphoma survivors – retrospective cohort analyses and a concept for prospective intervention. *International Journal of Cancer*, **124**, 1914–1917.

Keel, A., Bennett, B., Sarkar, T.K., Forman, K.M., Dawson, A.A. & Jones, P.F. (1983) Splenectomy and infection in Hodgkin's disease. *British Journal of Surgery*, **70**, 278–280.

Landgren, O., Bjorkholm, M., Konradsen, H.B., Soderqvist, M., Nilsson, B., Gustavsson, A., Axdorph, U., Kalin, M. & Grimfors, G. (2004) A prospective study on antibody response to repeated vaccinations with pneumococcal capsular polysaccharide in splenectomized individuals with special reference to Hodgkin's lymphoma. *Journal of Internal Medicine*, **255**, 664–673.

Lynch, A.M. & Kapila, R. (1996) Overwhelming postsplenectomy infection. *Infectious Disease Clinics of North America*, **10**, 693–707.

Mauch, P. & Somers, R. (1992) Controversies in the use of diagnostic staging laparotomy and splenectomy in the management of Hodgkin's disease. *Annals of Oncology*, **3**(Suppl. 4), 41–43.

Merk, K., Bjorkholm, M., Tullgren, O., Mellstedt, H. & Holm, G. (1990) Immune deficiency in family members of patients with Hodgkin's disease. *Cancer*, **66**, 1938–1943.

Swerdlow, A.J., Barber, J.A., Hudson, G.V., Cunningham, D., Gupta, R.K., Hancock, B.W., Horwich, A., Lister, T.A. & Linch, D.C. (2000) Risk of second malignancy after Hodgkin's disease in a collaborative British cohort: the relation to age at treatment. *Journal of Clinical Oncology*, **18**, 498–509.

Waghorn, D.J. (2001) Overwhelming infection in asplenic patients: current best practice preventive measures are not being followed. *Journal of Clinical Pathology*, **54**, 214–218.


# Temozolomide may induce therapy-related acute lymphoblastic leukaemia

Temozolomide (TMZ) is a second-generation oral alkylating agent that is approved for treatment of high-grade gliomas, such as anaplastic astrocytoma and glioblastoma multiforme. Administration of TMZ together with cranial radiotherapy after surgical removal of the glioblastoma is sufficiently tolerable and confers significant survival benefits, when compared with adjuvant radiotherapy alone (Stupp *et al*, 2005). Although traditional chemotherapy comprising procarbazine, lomustine (CCNU) and vincristine (PCV regimen) demonstrates comparable efficacy against high-grade gliomas (Brada *et al*, 2010), it has been replaced by TMZ because this drug has less myelotoxicity and is thus more applicable to the outpatient setting. On the other hand, previous exposure to alkylators is strongly associated with therapy-related myelodysplastic syndrome (t-MDS) and therapy-related acute myeloid leukaemia (t-AML) harbouring whole or partial losses of chromosomes 5 and 7, with frequent complex or hyperdiploid karyotype (Mauritzson *et al*, 2002). Because TMZ is a relatively new agent and because glioblastoma is an aggressive malignant neoplasm with a poor prognosis, TMZ-related haematological disorders have not yet been fully characterized. Herein we describe a case of glioblastoma who developed acute lymphoblastic leukaemia (ALL) after prolonged exposure to TMZ. In contrast to many other alkylating agents that cause secondary haematological neoplasms of the myeloid lineage, we found that TMZ-related leukaemia is predisposed to lymphoblastic phenotypes through a literature review.

A 49-year-old Japanese female with no remarkable medical history was diagnosed with grade II astrocytoma of the right temporal lobe and received surgical resection. Three years later, a follow-up magnetic resonance imaging scan revealed local recurrence. A craniotomy was performed and the recurrent tumour was largely resected except for the portion that infiltrated the insula. A re-craniotomy was performed due to post-operative intratumoural haemorrhage, and the patient subsequently developed left hemiparesis. A malignant transformation to glioblastoma was pathologically confirmed. Hence, the surgery was followed by cranial radiotherapy at a total dose of 80 Gy in 40 fractions. Adjuvant chemotherapy was commenced with TMZ for five consecutive days every 4 weeks. After the initial dose of 150 mg/m$^2$/d, the dose was increased to 200 mg/m$^2$ from the second cycle. This treatment was discontinued after 54 cycles due to leucopenia. Five months later, the patient was referred to our department, because leukaemic blasts had appeared in the peripheral blood. Her haemoglobin level was 101 g/l, leucocyte count $0{\cdot}8 \times 10^9$/l with 40% blasts, and platelet count $135 \times 10^9$/l. The bone marrow aspiration demonstrated hypercellular marrow with 88% myeloperoxidase-negative blasts, which were positive for CD10, CD19 and CD34 by flow cytometric analysis and also positive for nuclear terminal deoxynucleotidyl transferase (TdT) by immunohistochemical staining. Cytogenetic study showed normal karyotype in all 20 metaphases analysed. *BCR-ABL1* gene rearrangement was not detected by reverse

Table I. Characterization of Temozolomide-related acute lymphoblastic leukaemia.

| Author | Patient, age | Primary neoplasms | Radiation (Gy) | Latency* (months) | Cytogenetics | Immunophenotype (positive markers) |
|---|---|---|---|---|---|---|
| De Vita *et al* (2005) | Male, 40 years | Glioblastoma multiforme | 60 | 4 | 45, XY, −7, der(9)(p12) t(9;22) | Pre-B (CD10, CD19, CD22, CD34, CD45 and TdT) |
| Momota *et al* (2010) | Female, 12 years | Anaplastic astrocytoma | 60 | 13 | Normal karyotype | Pre-B (CD10, CD19, CD34, CD45, TdT and HLA-DR) |
| Shaikh and Masood (2010) | Male, 26 years | Mixed glioma (astrocytoma and oligodendroglioma) | 60 | 17 | Normal karyotype | Pre-T (CD3, CD5, CD7, CD45 and TdT) |
| Present report | Female, 49 years | Grade II astrocytoma → glioblastoma | 80 | 57 | Normal karyotype | Pre-B(CD10, CD19, CD34, CD45 and TdT) |

TdT, terminal deoxynucleotidyl transferase; pre-B, precursor B-cell; pre-T, precursor T-cell.
*Latency period between initial TMZ administration and onset of acute lymphoblastic leukaemia.

transcriptase-polymerase chain reaction assay. We therefore made a diagnosis of precursor B-cell ALL. Although complete remission was achieved after one course of induction chemotherapy with doxorubicin, vincristine, cyclophosphamide, asparaginase and prednisolone, a deteriorating performance status prevented her from receiving further treatments.

ALL has been reported to occur, although rarely, after chemotherapy or radiotherapy. In a large retrospective study by the Gruppo Italiano Malattie Ematologiche Maligne dell'Adulto (GIMEMA), 11 (1·2%) out of 901 ALL patients had a history of prior treatments (Pagano *et al*, 1999). This prevalence is much lower than that of t-MDS (13%) or t-AML (16%) (Mauritzson *et al*, 2002). Hence, it remains still controversial whether secondary ALL is truly 'therapy-related' or occurs by mere chance. A recent meta-analysis showed that topoisomerase II inhibitors have a causal relationship to secondary ALL with 11q23 aberrations (Shivakumar *et al*, 2008), indicating that at least some secondary ALL cases could be therapy-related. So far, no relationship has been demonstrated between alkylators and secondary ALL.

To our knowledge, 18 cases of secondary haematological neoplasms with prior TMZ exposure have been reported. Amongst them were 11 patients who had also been treated with other alkylators or topoisomerase II inhibitors and presented with t-MDS/t-AML. Notably, four out of seven patients who received TMZ alone were diagnosed with ALL (Table I). When Momota *et al* (2010) described the second case, they suggested the possibility that secondary haematological neoplasms after single-agent chemotherapy of TMZ might manifest as ALL. The subsequent two cases together support their notion and confirm that secondary ALL is a recurrent complication. As in the case of topoisomerase II inhibitors, it is likely that TMZ induces therapy-related ALL.

TMZ-related ALL may be characterized by normal karyotype and precursor B-cell immunophenotype. Chromosomal abnormalities were detected in only a single case that exhibited the Philadelphia chromosome and deletion of chromosome 5. In three patients, lymphoblasts presented precursor B-cell immunophenotype with positive expression of CD10, CD19, CD34 and TdT, whilst precursor T-cell immunophenotype was noted in the other case. The median time latency between the initial TMZ administration and the onset of ALL was 15 months (range 4–57), much shorter than that between traditional alkylators and t-MDS/t-AML (63 months) (Mauritzson *et al*, 2002). It is principally attributed to the shortened survival due to glioblastoma.

Patients with high-grade gliomas almost inevitably receive adjuvant cranial radiotherapy. Because the skull contains 7–28% of whole active bone marrow, depending on age, we need to also consider the effect of radiotherapy on secondary leukaemia. In treatment of childhood ALL, cranial radiotherapy did not raise the cumulative incidence of secondary AML (0·6% vs. 0·6%), whereas it resulted in a significantly higher risk of overall secondary neoplasms (3·5% vs. 1·2%) (Löning *et al*, 2000). Moreover, out of 28 adult patients with t-AML following primary brain neoplasms, 27 patients received PCV-based chemotherapy as well as radiotherapy (Perry *et al*, 1998). Taken together, these findings indicate that cranial radiotherapy seems to confer a limited influence, and thus it is likely that TMZ plays a dominant role in the pathogenesis of TMZ-related leukaemia.

Finally, TMZ is being adopted in clinical trials for various malignant neoplasms. The present report demonstrates that it is important to be aware of the potential of TMZ-related ALL.

## Conflict of interest

The authors have no conflicts of interest.

**Mizuki Ogura**[1]
**Tomoki Todo**[2,3]
**Minoru Tanaka**[3]
**Yasuhito Nannya**[1]
**Motoshi Ichikawa**[1]
**Fumihiko Nakamura**[1]
**Mineo Kurokawa**[1,4]

[1]Department of Haematology & Oncology, Graduate School of Medicine, University of Tokyo, [2]Translational Research Centre, University of Tokyo Hospital, [3]Department of Neurosurgery, Graduate School of Medicine, University of Tokyo, and [4]Department of Cell Therapy and Transplantation Medicine, University of Tokyo Hospital, Tokyo, Japan.
E-mail: kurokawa-tky@umin.ac.jp

Keywords: acute lymphoblastic leukaemia, alkylating agent, glioblastoma, temozolomide, therapy-related.

First published online 26 April 2011
doi: 10.1111/j.1365-2141.2011.08641.x

## References

Brada, M., Stenning, S., Gabe, R., Thompson, L.C., Levy, D., Rampling, R., Erridge, S., Saran, F., Gattamaneni, R., Hopkins, K., Beall, S., Collins, V.P. & Lee, S.M. (2010) Temozolomide versus procarbazine, lomustine, and vincristine in recurrent high-grade glioma. *Journal of Clinical Oncology*, **28**, 4601–4608.

De Vita, S., De Matteis, S., Laurenti, L., Chiusolo, P., Reddiconto, G., Fioritoni, A., Leone, G. & Sica, S. (2005) Secondary Ph+ acute lymphoblastic leukemia after temozolomide. *Annals of Hematology*, **84**, 760–762.

Loning, L., Zimmermann, M., Reiter, A., Kaatsch, P., Henze, G., Riehm, H. & Schrappe, M. (2000) Secondary neoplasms subsequent to Berlin-Frankfurt-Munster therapy of acute lymphoblastic leukemia in childhood: significantly lower risk without cranial radiotherapy. *Blood*, **95**, 2770–2775.

Mauritzson, N., Albin, M., Rylander, L., Billström, R., Ahlgren, T., Mikoczy, Z., Björk, J., Strömberg, U., Nilsson, P.G., Mitelman, F., Hagmar, L. & Johansson, B. (2002) Pooled analysis of clinical and cytogenetic features in treatment-related and de novo adult acute myeloid leukemia and myelodysplastic syndromes based on a consecutive series of 761 patients analyzed 1976–1993 and on 5098 unselected cases reported in the literature 1974–2001. *Leukemia*, **16**, 2366–2378.

Momota, H., Narita, Y., Miyakita, Y., Hosono, A., Makino, K. & Shibui, S. (2010) Acute lymphoblastic leukemia after temozolomide treatment for anaplastic astrocytoma in a child with a germline TP53 mutation. *Pediatric Blood & Cancer*, **55**, 577–579.

Pagano, L., Pulsoni, A., Tosti, M.E., Annino, L., Mele, A., Camera, A., Martino, B., Gugliemi, C., Cerri, R., Di Bona, E., Invernizzi, R., Castagnola, C., Bassan, R., Mele, L., Fodeschini, G., Leone, G. & Mandelli, F. (1999) Acute lymphoblastic leukaemia occurring as second malignancy: report of the GIMEMA archive of adult acute leukaemia. Gruppo Italiano Malattie Ematologiche Maligne dell'Adulto. *British Journal of Haematology*, **106**, 1037–1040.

Perry, J.R., Brown, M.T. & Gockerman, J.P. (1998) Acute leukemia following treatment of malignant glioma. *Journal of Neuro-Oncology*, **40**, 39–46.

Shaikh, A.I. & Masood, N. (2010) Acute lymphoblastic leukemia subsequent to temozolomide use in a 26-year-old man: a case report. *Journal of Medical Case Reports*, **4**, 274.

Shivakumar, R., Tan, W., Wilding, G.E., Wang, E.S. & Wetzler, M. (2008) Biologic features and treatment outcome of secondary acute lymphoblastic leukemia–a review of 101 cases. *Annals of Oncology*, **19**, 1634–1638.

Stupp, R., Mason, W.P., van den Bent, M.J., Weller, M., Fisher, B., Taphoorn, M.J.B., Belanger, K., Brandes, A.A., Marosi, C., Bogdahn, U., Curschmann, J., Janzer, R.C., Ludwin, S.K., Gorlia, T., Allgeier, A., Lacombe, D., Cairncross, J.G., Eisenhauer, E. & Mirimanoff, R.O., European Organisation for Research and Treatment of Cancer Brain Tumor and Radiotherapy Groups; National Cancer Institute of Canada Clinical Trials Group (2005) Radiotherapy plus concomitant and adjuvant temozolomide for glioblastoma. *New England Journal of Medicine*, **352**, 987–996.

# Homozygously deleted gene DACH1 regulates tumor-initiating activity of glioma cells

Akira Watanabe[a,b,1], Hideki Ogiwara[a,c,1], Shogo Ehata[d], Akitake Mukasa[c], Shumpei Ishikawa[a,e], Daichi Maeda[e], Keisuke Ueki[f], Yasushi Ino[c], Tomoki Todo[c], Yasuhiro Yamada[b], Masashi Fukayama[e], Nobuhito Saito[c], Kohei Miyazono[d], and Hiroyuki Aburatani[a,g,2]

[a]Genome Science Division, Research Center for Advanced Science and Technology, University of Tokyo, Tokyo 153-8904, Japan; [b]Department of Reprogramming Science, Center for iPS Research and Application, Kyoto University, Kyoto 606-8507, Japan; Departments of [c]Neurosurgery, [d]Molecular Pathology, and [e]Human Pathology, Graduate School of Medicine, University of Tokyo, Tokyo 113-0033, Japan; [f]Department of Neurosurgery, Dokkyo University Medical School, Tochigi 321-0293, Japan; and [g]Core Research for Evolutional Science and Technology, Japan Science and Technology Agency, Saitama 332-0012, Japan

Edited* by Charles R. Cantor, Sequenom, Inc., San Diego, CA, and approved June 1, 2011 (received for review June 22, 2009)

**Loss or reduction in function of tumor suppressor genes contributes to tumorigenesis. Here, by allelic DNA copy number analysis using single-nucleotide polymorphism genotyping array and mass spectrometry, we report homozygous deletion in glioblastoma multiformes at chromosome 13q21, where *DACH1* gene is located. We found decreased cell proliferation of a series of glioma cell lines by forced expression of DACH1. We then generated U87TR-Da glioma cells, where DACH1 expression could be activated by exposure of the cells to doxycycline. Both ex vivo cellular proliferation and in vivo growth of s.c. transplanted tumors in mice are reduced in U87TR-Da cells with DACH1 expression (U87-DACH1-high), compared with DACH1-nonexpressing U87TR-Da cells (U87-DACH1-low). U87-DACH1-low cells form spheroids with CD133 and Nestin expression in serum-free medium but U87-DACH1-high cells do not. Compared with spheroid-forming U87-DACH1-low cells, adherent U87-DACH1-high cells display lower tumorigenicity, indicating DACH1 decreases the number of tumor-initiating cells. Gene expression analysis and chromatin immunoprecipitation assay reveal that fibroblast growth factor 2 (FGF2/bFGF) is transcriptionally repressed by DACH1, especially in cells cultured in serum-free medium. Exogenous bFGF rescues spheroid-forming activity and tumorigenicity of the U87-DACH1-high cells, suggesting that loss of DACH1 increases the number of tumor-initiating cells through transcriptional activation of bFGF. These results illustrate that DACH1 is a distinctive tumor suppressor, which does not only suppress growth of tumor cells but also regulates bFGF-mediated tumor-initiating activity of glioma cells.**

neural differentiation | gliomagenesis

Glioblastoma multiformes (GBMs), the most frequent primary malignant brain tumor in adults, are aggressive and highly invasive tumors (1). Genetic alterations of GBMs, including aberration of DNA copy number such as gene amplifications, loss of heterozygosity (LOH), and homozygous deletions, leads to activation of oncogenes and inactivation of tumor suppressor genes (1–3). DNA copy number analysis by single-nucleotide polymorphism (SNP) genotyping enables the high-resolution analysis of allelic DNA copy number and has been used to obtain a genome-wide view of DNA copy number alterations in human cancers (4–10). Particularly, pairwise analysis of normal and tumor DNAs is crucial in detecting homozygous deletion in clinical specimens, because infiltrating nontumorous cells are significant in GBMs.

In this study we examined the allelic copy number of paired glioma and blood DNAs by SNP genotyping array analysis by using Genome Imbalanced Map (GIM) algorithm (5, 11), which could calculate the signal ratio of SNP genotyping array in an allelic manner. We identified a unique homozygous deletion at *DACH1* gene region on chromosome 13q21, and we demonstrated forced expression of DACH1 reduced proliferation of cultured glioma cells and in vivo tumor growth in ortholotopic xenograft model. We also found that DACH1 inhibited formation of tumor-initiating spheroids, presumably by directly repressing expression of fibroblast growth factor-2 (*FGF2*), suggesting *DACH1* is a unique tumor suppressor of glioblastoma, which not only suppresses tumor growth but also inhibits generation of tumor-initiating cells.

## Results

**DACH1 Gene on Chromosome 13q21 Is Homozygously Deleted in Glioblastoma.** To identify genomic alterations involved in gliomagenesis, we performed DNA copy number analysis of eight GBMs by using SNP genotyping array (Fig. 1*A* and Fig. S1*A*), as well as analysis of a corresponding normal blood DNA for highlighting tumor-specific alterations. We observed high-level amplification at chromosome 7q21 (inferred total copy number >8) and copy number reduction within chromosome arm 4q, 10p, 13q, 16q, 17q, and 18q, and we detected homozygously deleted loci at chromosome 9q21 and 10q23, which spanned known tumor suppressor genes *CDKN2A* and *PTEN*, respectively. In addition, we found a unique homozygous deletion at chromosome 13q21 in GBM case 4 and LOH at the region in GBM case 1 and 3 (Fig. 1*A* and Fig. S1*A*). Although loss of chromosome 13q14.2 spanning *RB1* gene is frequently observed in human malignancies including GBMs (12, 13), the homozygous deletion of chromosome 13q21 has not been reported.

To examine allelic DNA copy numbers at the chromosome 13q21 region in additional GBM cases, we performed targeted genotyping analysis of 28 paired GBMs and blood cells by high-density mass spectrometric analysis using MassARRAY (14, 15). The chromosomal losses were found at least in 11 samples (GBM case 1, 3, 4, 5, 18, 19, 24, 25, 26, 27, and 28; 39.3%), and three of them (GBM case 4, 5, and 27; 10.7% of GBMs) displayed homozygous deletion (Fig. 1*B* and Fig. S1*B*). By combination of SNP genotyping array with MassARRAY analysis, homozygously deleted region at chromosome 13q21 of GBM case 4 was restricted to rs1999603 (probe S10)–rs1326684 (probe M8), which might be extended from rs9542598 (probe M2) to rs1421280 (probe S15). In two additional GBM cases, homozygous deletions found by MassARRAY at this locus were from rs10492537 (probe M6) to rs3818437 (probe M7), which might be extended

Author contributions: A.W. and H.A. designed research; A.W., H.O., S.E., A.M., D.M., Y.Y., and K.M. performed research; S.E., A.M., K.U., Y.I., T.T., M.F., and N.S. contributed new reagents/analytic tools; A.W. and S.I. analyzed data; and A.W., A.M., and H.A. wrote the paper.

The authors declare no conflict of interest.

*This Direct Submission article had a prearranged editor.

[1]A.W. and H.O. contributed equally to this work.

[2]To whom correspondence should be addressed: E-mail: haburata-tky@umin.ac.jp.

This article contains supporting information online at www.pnas.org/lookup/suppl/doi:10.1073/pnas.0906930108/-/DCSupplemental.

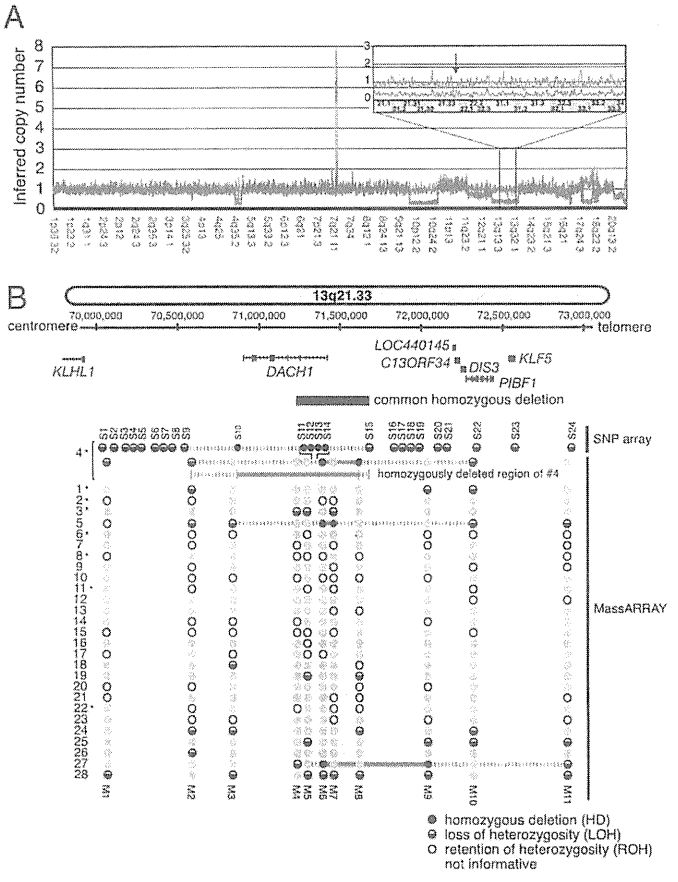


Fig. 1. DACH1 is homozygously deleted in GBMs. (*A*) An integrated view of DNA copy numbers and allelic alternations of GBM case 4. Scatter plot of inferred allelic copy numbers (red and blue) was estimated by GIM algorithm. An arrow indicated homozygously deleted loci. (*Right*) Magnified view of DNA copy number of GBM case 4 from chromosome 13q21 to 13q34. One allele showed DNA copy number reduction in whole region (blue), whereas the other allele (red) showed copy number reduction only at chromosome 13q21. (*B*) Summary of SNP genotyping in the 13q21 region. S1-24 and M1-11 are SNP ID available in SNP genotyping array and MassARRAY, respectively. Black line, the homozygously deleted region; dotted line, the possible extended region of homozygous deletions; *, also examined by SNP arrays shown in Fig. S1*A*.

to rs1931443 (probe M3)–rs7332388 (probe M10) in GBM case 5, and from rs10492537 (probe M6) to rs1981186 (probe M9), which might be extended to rs10507796 (probe M4)–rs1886452 (probe M11) in GBM case 27. The boundary of the common homozygously deleted region on the centromeric side was estimated at rs10507796 (probe M4), which was genotyped as LOH in case 27, whereas the telomeric boundary was estimated at rs1421280 (probe S15), which was genotyped as LOH in case 4 (Fig. 1*B*). Because the homozygously deleted region from rs10507796 to rs1421280 overlapped with *DACH1* gene and did not span the adjacent genes to *DACH1* such as *LOC440145* and *KLHL1*, we thought *DACH1* was a target of these deletions and could be a potential candidate as a tumor suppressor gene of GBMs. Quantitative PCR analysis demonstrated that DNA copy numbers of GBM samples with a homozygous deletion at *DACH1*-region were much lower than that of whole brain and normal fibroblast cells KMS-6, which has a normal karyotype as (46, XX) (Fig. S2*A*). In addition, we confirmed protein expression of DACH1 was reduced in glioma cells with a homozygous deletion at *DACH1* region, whereas it was detectable in vascular endothelial cells (Fig. S2*B*).

**DACH1 Expression Reduces Growth of Glioma Cells.** We screened an expression level of *DACH1* gene in a series of glioma cell lines. Forced expression of lentivirus-carrying *DACH1* reduced cell proliferation of SF188, U87MG, T98G, and LNG-308 glioma cell lines, where endogenous expression of *DACH1* was not detectable (Fig. S3 *A* and *B*). We then generated two U87MG-derived cell lines: U87TR-Da clone-16 and -18, where DACH1 expression could be induced by the addition of doxycycline (Fig. 2*A* and Fig. S4*A*). DACH1 decreased viability of the cells at 4 and 6 d after addition of doxycycline (Fig. 2*B*) and also abrogated anchorage-independent growth of the cells in soft agar (Fig. S3 *C* and *D*). We next examined the impact of DACH1 expression on in vivo growth of s.c.-injected tumors of U87TR-Da clone-16 and -18. Increased expression of DACH1 was observed at 8 d after replacement of doxycycline-free drinking water by doxycycline-supplemented water (Fig. 2 *C* and *D*). Growth of the U87TR-Da clone-16 and clone-18 tumors was significantly decreased by administration of doxycycline compared with U87TR-Da tumors supplemented with normal drinking water (Fig. 2 *E* and *F* and Fig. S4*B*). Tumor formation was reproduced by stereotactic intracerebral inoculation of DACH1-nonexpressing U87TR-Da cells, whereas tumor was not detectable by the injection of DACH1-expressing U87TR-Da cells (Fig. 2 *G* and *H* and Fig. S3*E*). These results demonstrated that *DACH1* decreased growth and proliferation of glioma cells both ex vivo and in vivo, supporting that *DACH1* is a tumor suppressor gene of GBMs.

**DACH1 Inhibits Formation of Tumor-Initiating Spheroids of Glioma Cells.** DACH1 is structurally related to c-Ski and SnoN, which act as transcriptional repressors of the transforming growth factor-β (TGF-β) signaling pathway through the interaction with Smad proteins (16). Previous studies showed that human DACH1 inhibited TGF-β signaling through repressing cyclin D1 (*CCND1*) expression and decreased proliferation of breast cancer cells (17, 18). We examined whether DACH1 expression affected TGF-β signaling in glioma cells. Induced DACH1 expression reduced the proliferation of the U-373MG cells, which are widely used as a cell model for analyzing TGF-β signaling (19), and repressed TGF-β3–stimulated $(CAGA)_9$- and p800-luciferase activity (Fig. S5 *A*–*C*). However, the expression of cyclin D1, which was proposed as a transcriptional target of DACH1 in breast cancer cell lines (18), was not affected by induced expression of DACH1 (Fig. S5*D*). Because DACH1 might repress expressions of the other target genes, but except for cyclin D1, we sought DACH1-regulated genes, which could affect growth of glioma cells. By global expression analysis of DACH1-high and -low cells, we found *FGF2* expression was repressed by DACH1 (Table S1, Fig. 3*A*, and Fig. S4*A*). Because FGF2, also named basic FGF (bFGF), is an essential factor for maintenance of self-renewal of glioma-initiating cells (20, 21), we thought DACH1 affected manintenance of self-renewal of glioma-initiating cells. We discovered DACH1, grown in serum-free neurobasal (NBE) medium (22), blocked spheroid formation of U87TR-Da cells, whereas cell morphology in serum-containing medium was not changed by DACH1 expression (Fig. 3*B*). Because glioma-initiating cells have been proposed to form spheroids (21), we thought that DACH1-nonexpressing U87TR-Da cells, which formed spheroids in NBE medium, showed high tumorigenicity compared with DACH1-expressing U87TR-Da cells in NBE medium. We confirmed that spheroid of DACH-nonexpressing cells cultured in NBE medium showed high expression of *CD133*, which has been reported as a marker of cells that are capable of tumor initiation (21), and a neural stem cell marker Nestin (Fig. 3 *C* and *D*). We then performed s.c. injection of U87TR-Da cells to examine the relationship between spheroid formation and tumorigenicity of the cells. We found tumor formation of DACH1-nonexpressing U87TR-Da cells (3 of 4 mice with $5 \times 10^3$ cells and all mice with $2 \times 10^4$ and $1 \times 10^5$ cells), whereas DACH1-

GENETICS

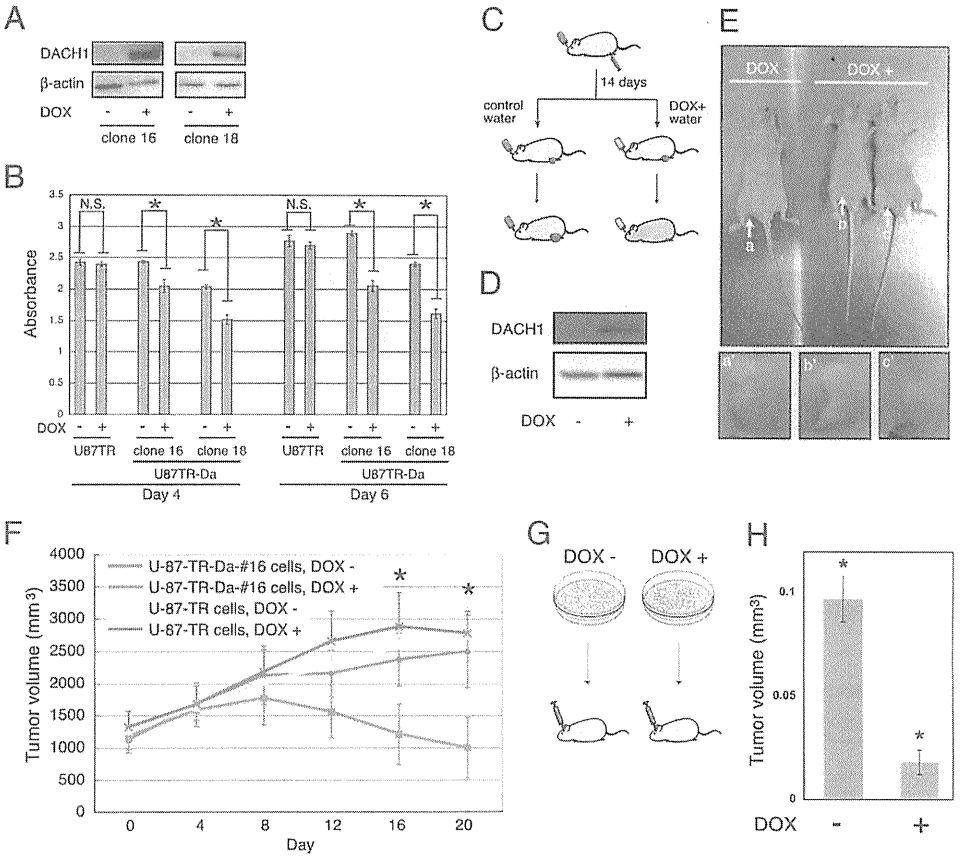


Fig. 2. DACH1 expression repressed growth of glioma cells. (*A*) Immunoblotting of U87TR-Da clone-16 and clone-18 cells with an anti-DACH1 antibody. (*B*) Cell proliferation of U87TR-Da cells, counted by WST-8 assay at 4 or 6 d after induction of *DACH1* by doxycycline. (*C*) Experimental model of tumor progression affected by DACH1 expression. Serially diluted U87TR-Da cells were injected s.c. into the backs of BALB/c nude mice, and the tumor formation was observed at 28 d after s.c. injection of the cells. (*D*) Expression of DACH1 in U87TR-Da tumor. DACH1 was detected by immunoblotting of xenografted U87TR-Da clone-16 tumors with an anti-DACH1 antibody (*Upper*). Tumor tissues were resected from mice drinking doxycycline-supplemented (left lane) or control water (right lane). β-actin was detected as a loading control (*Lower*). (*E*) Tumor formation of xenografted DACH1-nonexpressing or -expressing U87TR-Da clone-16 cells at 20 d after inoculation. (*F*) Growth of xenografted U87TR-Da clone-16 or U87TR tumors. DOX, doxycycline (1 μg/mL); points, mean ($n = 6$); bars, SEM of 6 amimals on per group; N.S., not statistically significant; $^*P < 0.05$ (two-way ANOVA), statistically significant compared with doxycycline minus control. (*G*) Orthotopic xenograft model for assessing the effect of DACH1 expression on tumor progression. U87TR-Da clone-16 cells were precultured in doxycycline-free (*Left*) or doxycycline-containing (*Right*) medium. (*H*) Size of tumors of the brain stereotactically implanted with DACH1-nonexpressing (DOX-) or -expressing (DOX+) cells at 5 wk after implantation. Bars, SEM of 4 amimals per group; N.S., not statistically significant; $^*P < 0.05$ (two-way ANOVA), statistically significant compared with doxycycline minus control.

expressing U87TR-Da cells did not form any tumors (Fig. 3*E*). Because DACH1-expressing U87TR-Da cells in serum-containing DMEM did not form tumors with so few cells ($2 \times 10^4$ to $1 \times 10^5$ cells), tumor-initiating cells might be enriched in spheroids of DACH1-nonexpressing U87TR-Da cells grown in serum-free NBE medium.

**FGF2 Rescues DACH1-Repressed Tumorigenicity.** *FGF2* expression was highly induced under serum-free culture condition, however, DACH1 repressed *FGF2* expression at low levels (Fig. 4*A*). We verified that DACH1 reduced a reporter activity of luciferase cis-regulated by *FGF2* promoter (Fig. S6*A*) and directly bound to FGF2 promoter region in DACH1-expressing U87TR-Da cells cultured in both serum-containing DMEM and serum-free NBE medium by ChIP analysis with an anti-DACH1 antibody (Fig. S6*B*). Because overexpression of *FGF2* was frequently observed in high-grade gliomas and involved in malignant progression of gliomas (23, 24) and a previous study showed that bFGF enhanced tumor-initiating spheroid formation of glioma cells (20), we examined whether spheroid formation of DACH1-expressing U87TR-Da cells was enhanced by exposure of cells to bFGF. DACH1-expressing U87TR-Da cells did not form spheroid, but exogenous bFGF-induced spheroid formation of DACH1-expressing U87TR-Da cells, indicating that bFGF, which was repressed by DACH1, increased the number of spheroid-forming tumor-initiating cells (Fig. 4*B* and Fig. S4*C*). Morphology of primary tumor spheroid, which did not express *DACH1*, was not markedly different under culture conditions with or without bFGF. However, by lentiviral expression of DACH1, the spheroid formation was partially disrupted, and most spheroid-forming cells started to differentiate even under bFGF-supplemented condition (Fig. S4*D*). We confirmed the reduced expression of a glioma stem cell marker CD133 in primary tumor-derived cells with DACH1 expression under both bFGF2-supplemented and -unsupplemented culture conditions (Fig. S4*E*). To examine whether bFGF overexpression can confer an increased tumorigenicity, the intracerebral implantation of the cells ectopically overexpressing DACH1 and FGF2 was performed (Fig. 4*C*). Tumor formation in DACH1-expressing cells with ectopic expression of FGF2 was much higher than that in control DACH1-expressing cells, showing that rescue of FGF2 repression in DACH1-expressing cells increases intracerebral tumor formation (Fig. 4 *D* and *E* and Fig. S6*C*). These results suggested that DACH1 suppress tumor formation through transcriptional repression of *FGF2*.

## Discussion

Loss of chromosome 13q has been reported to occur frequently in GBMs (12, 25, 26). Homozygous deletions, LOH, and mutations in *RB1* gene, which is located at chromosome 13q14.2, 23 Mb centromeric to *DACH1*, are found in human cancers including GBMs (13, 26). In this study, we found another locus with a homozygous deletion at 13q21 by SNP genotyping array and targeted genotyping analysis with a mass spectrometer. A previous study reported LOH of chromosome 13q was more common in secondary than in primary glioblastomas (3), and the mutations of *IDH1* and *IDH2* genes have suggested to associate with development of secondary glioblastomas (27–30). However, because significant relationship between loss of *DACH1* and mutations of *IDH1* and *IDH2* were not found, we think that the mechanisms of *DACH1* loss and gliomagenesis categorized into primary or secondary glioblastoma are different (Table S2).

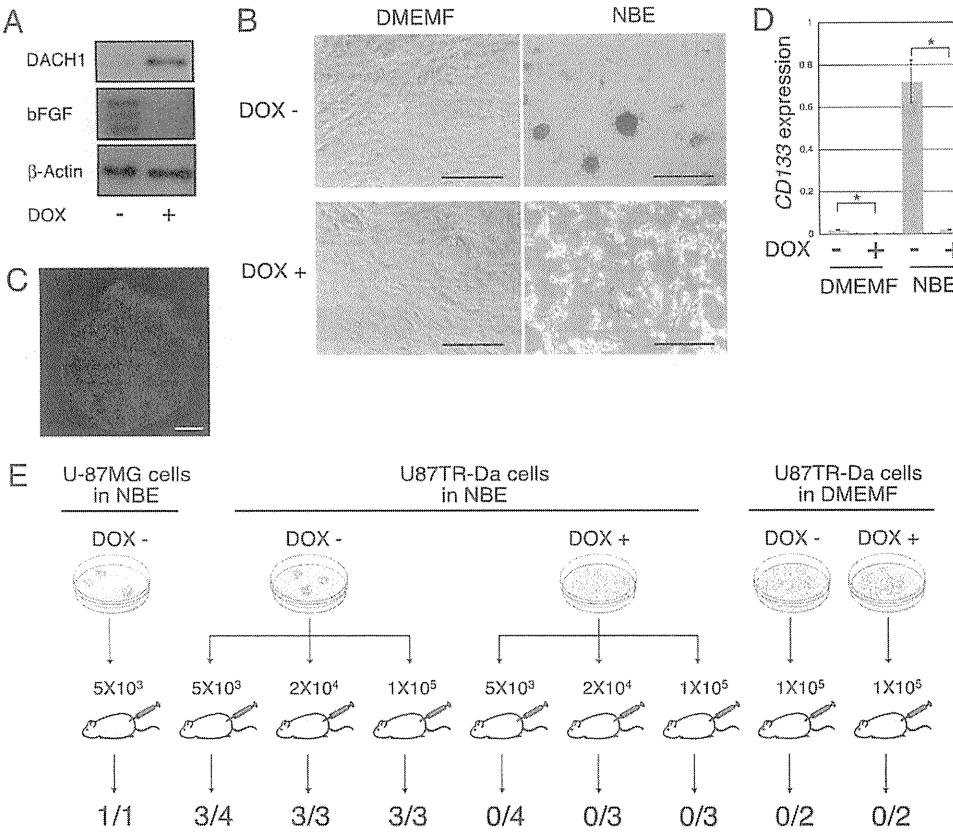


Fig. 3. Spheroid formation was inhibited by DACH1 expression. (*A*) Protein expression levels of DACH1 and bFGF in U87TR-Da clone-16 cells. (*B*) Images of cultured cells. U87TR-Da clone-16 cells were first cultured in FBS-containing DMEM in the absence (*Upper Left*) or presence (*Lower Left*) of doxycycline for 72 h, and then culture medium was replaced into serum-free NBE or serum containing DMEMF medium. Branched projection of adherent cells was observed in DACH1-nonexpressing cells (red arrows). (Scale bars: 500 μm.) (*C*) Nestin staining of spheroid (green). Nucleus was stained with DAPI (blue). (*D*) CD133 expression of DACH1-nonexpressing (DOX-) or -expressing (DOX+) cells under serum-containing (DMEMF) or serum-free (NBE) culture condition. Columns, mean ($n = 3$); bars, S.D.; *, **$P < 0.05$. (*E*) Tumor formation of DACH1-expressing or DACH1-nonexpressing U87TR-Da cells cultured in NBE medium. Tumor formation in 3 of 4 mice with $5 \times 10^3$ DACH1-nonexpressing U87TR-Da clone-16 cells and in all mice with $2 \times 10^4$ and $1 \times 10^5$ DACH1-nonexpressing U87TR-Da clone-16 cells was observed, whereas s.c. injection of DACH1-expressing U87TR-Da clone-16 cells did not form any tumors. DOX-, mice with U87TR-Da clone-16 cells cultured in doxycycline-free NBE medium; DOX+, mice with U87TR-Da cells cultured in doxycycline-supplemented medium.

*DACH1*-spanning region is indicated as a target of copy number variations (CNV), where healthy individuals also exhibit copy number changes. Although it is hard to detect tumor-specific small deletions by a general copy number analysis using an algorithm based on moving window, our GIM algorithm can normalize aberrant copy number change even in CNV region by using signal data of both tumor DNA and corresponding normal DNA (4, 11). We overcame CNV effect and could detect small homozygous deletions at DACH1 region by an improved algorithm for SNP genotyping array with the targeted genotyping analysis using a mass spectrometer.

To explore additional mechanisms for *DACH1* inactivation other than genomic loss, we first examined sequencing of *DACH1* exonic regions by using genomic DNA from 25 GBM tumors and 8 glioma cell lines and did not observe any somatic mutations, whereas GBM case 25 showed LOH and the remained allele with nonsynonymous polymorphism, which could be translated into amino acid-substituted DACH1, V464M (Fig. S2*C*). It should require further examination such as loss-of-function of the protein and frequency of mutational events with amino acid substitution of DACH1 protein in GBMs. We then examined methylation status of *DACH1* promoter region, because a CpG island existed in the vicinity of transcription start site (TSS) of *DACH1*. Because DNA hypermethylation at *DACH1* promoter region was frequently observed (Fig. S2*D*), hypermethylation of the *DACH1* promoter could be an additional mechanism for DACH1 inactivation in gliomagenesis.

Homozygous deletions observed in all three cases contained a deduced promoter region and the first exon with ATG start codon of *DACH1* gene, indicating the homozygous deletions cause functional disruption of DACH1. Forced expression of DACH1 decreases growth of glioma cells and inhibits formation of spheroids, which are proposed as a tumor-initiating cell population and chemoresistant population of glioma cells. Even though downstream signaling of bFGF is well described, only a few reports have provided the mechanism of transcriptional regulation of *FGF2* (31, 32). Here, we demonstrated that DACH1, a member of corepressor complexes, repressed *FGF2* expression. Campanelli et al. found the expression level of DACH1 in glial precursors was much higher than that in neural stem cells (NSCs) (33). Withdrawal of bFGF, which is known as a critical component of culture medium for human embryonic and neural stem cells (34), drives astrocytic differentiation (2, 34, 35). So we think that loss or mutation of DACH1 may interrupt astrocytic differentiation of glial-restricted progenitor cells through sustained expression of bFGF and, subsequently, trigger gliomagenesis by convertion of progenitor cells to tumor-initiating cells.

Although loss of *DACH1* was detected in some GBM specimens and glioma cell lines at genomic and/or transcriptional level, there were other glioma cell lines that exhibited detectable DACH1 expression, such as U251MG (Fig. S3*A*). When we silenced *DACH1* expression of U251MG by RNA interference (RNAi) (Fig. S7*A*), slightly increased cell proliferation was observed (Fig. S7*B*). *FGF2* and *CD133* expression was slightly upregulated when *DACH1* expression was silenced by RNAi (Fig. S7 *C* and *D*). We also observed increased spheroid formation in *DACH1*-silenced cells under serum-free culture condition (Fig. S7*E*). However, these effects of *DACH1* silencing in U251MG cells were relatively slight. Because U251MG exhibited cell-autonomous growth even with high DACH1 expression, there must be additional alterations in oncogenes/tumor suppressor genes other than *DACH1*, which might obscure the effect of *DACH1* silencing on tumor suppressing activity.

In the analysis with expression microarrays, we observed that DACH1 decreased expression of secreted factors including TGF-β2, leukemia inhibitory factor (LIF), and interleukin-6 (IL-6) (Table S1). Recent reports demonstrated that TGF-β enhanced the self-renewal property of glioma-initiating cells by activating

GENETICS

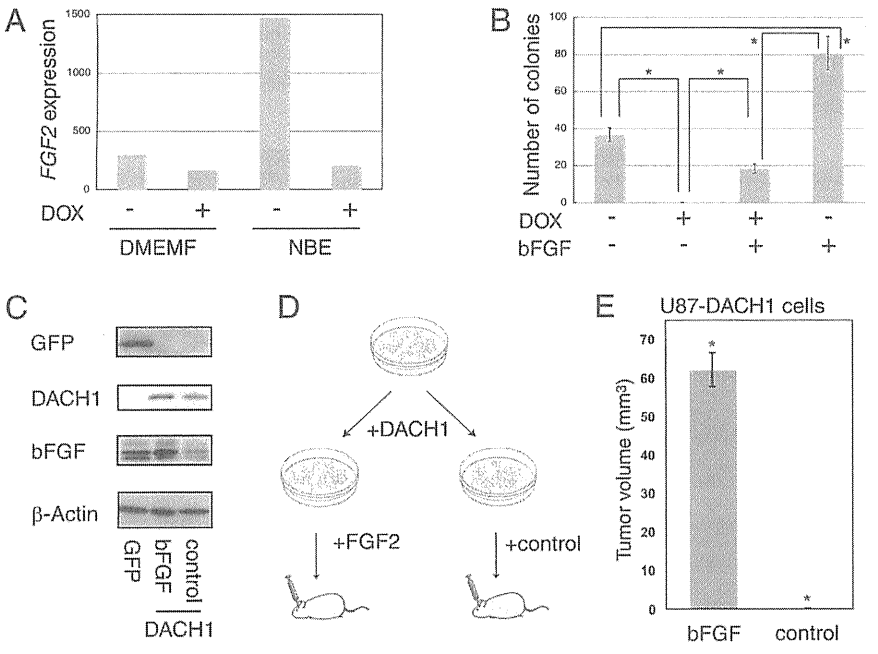


Fig. 4. Ectopic DACH1 expression decreases FGF2 expression, spheroid formation, and tumor growth. (*A*) Repressed *FGF2* expression by DACH1. DMEMF, serum-containing DMEM; NBE, serum-free Neurobasal medium. (*B*) Spheroid formation in U87TR-Da in the absence and presence of bFGF. Columns, mean ($n$ = 3); bars, SEM of three experiments; $^*P < 0.05$ (unpaired $t$-test), statistically significant compared with doxycycline minus control. (*C*) Protein expression of green fluorescent protein (GFP), DACH1, and bFGF. (*D*) Orthotopic xenograft model for assessing the effect of *FGF2* on tumor progression of *DACH1*-expressing cells. U87MG cells were lentivirally transduced with DACH1 and cultured in zeocin-containing medium. Then, DACH1-expressing cells were infected with lentivirus carrying FGF2 (*Left*) or control (*Right*) vector. (*E*) Size of tumors of the brain implanted with *FGF2*-expressing or control U87MG cells. Bars, SEM of 5 amimals on per group; N.S., not statistically significant; $^*P < 0.05$ (two-way ANOVA), statistically significant compared with doxycycline minus control.

LIF-JAK/STAT pathway (36), and autocrine TGF-β signaling is involved in maintenance of tumorigenicity of glioma-initiating cells (19). Both LIF and IL-6 also are activators of JAK/STAT pathway. So we presumed that DACH1 may suppress tumorigenesis through repression of not only *FGF2* but also the above tumor-initiating factors. Potential tumor-initiating factors, such as bFGF, TGF-β, LIF, and IL-6, will also be good candidates drug targets for GBMs.

The previous integrated genomic analysis of glioblastoma identified genomic alterations in genes belonging not only to a variety of cellular process pathways, which were likewise altered in many types of cancers, but also to nervous system-specific cellular pathways (27). From our results, we think that *DACH1* may function as one of tumor suppressor genes regulating through nervous system-specific cellular pathways. Little is yet known about the origin of glioblastoma cells, but some reports suggested that NSCs in the subventricular zone (SVZ) of the adult brain might be a candidate origin of cancer stem cells of glioblastoma (37, 38). Although we could not detect DACH1 expression at adult SVZ, a high expression of DACH1 was observed at the ventricular wall of fetus (Fig. S2 *E* and *F*), implicating involvement of DACH1 in maturation of neural cells. Li and colleagues demonstrated murine Dach1 regulated retinogenesis and pituitary development through tissue-specific gene regulation by recruiting the corepressors (39, 40). Functional relevance of *DACH1* expression in development and neural differentiation of both invertebrates and vertebrates has been reported (39–46). DACH1-expressed embryonic and postnatal brain-derived cells displayed neural stem cell-like property (44), suggesting that DACH1 functions in neural differentiation. From these facts together, we think that DACH1 act as a guardian of differentiation in the glial lineage, and loss of DACH1 would result in dysregulation of normal differentiation and drive gliomagenesis.

Taking advantages of our allelic DNA copy number analysis for tumors and corresponding normal cells by using SNP genotyping array as well as MassARRAY, we provide evidence that DACH1 is homozygously deleted in GBMs. As far as we know, this is the first study showing loss of DACH1 gene function in tumor cells at the genomic level. Our observation supports recent studies indicating that DACH1 scarcely expressed in tumor-initiating cells and such low expression correlated with poor prognosis of breast cancers (17, 18, 47). We showed that DACH1 expression decreases proliferation of glioma cells and suppresses tumorigenicity through inhibition of bFGF-dependent spheroid formation. We here propose DACH1 is a unique tumor suppressor gene, which does not only suppresses tumor growth but also inhibits generation of tumor-initiating cells during neural differentiation. Understanding molecular basis of DACH1-mediated epigenetic regulation may provide mechanism of both neural differentiation and gliomagenesis.

## Methods

**Materials.** All clinical samples were obtained with the informed consent of the patients after permission by the ethics committees of Tokyo University Hospital. Tumors were diagnosed according to World Health Organization classification (48).

**SNP Genotyping Array.** SNPs of peripheral blood cells or GBM samples were genotyped by 50K Xba SNP mapping arrays (Affymetrix) according to GeneChip Mapping 50K Assay Manual (4). Allelic and total DNA copy numbers were calculated by GIM algorithm (11).

**MassARRAY Analysis.** SNP genotyping of 28 GBM samples, including the 8 samples used in the initial screening by SNP mapping array analysis, was performed with MassARRAY Genotyping system (Sequenom). Paired DNA samples from blood or tumor were genotyped in duplicate. Quantitation of the peak area was performed by Sequenom's MassARRAY RT software. The threshold for LOH was defined as 40% reduction of one allele in tumor sample, as described (14).

**Gene Expression Analysis.** Total RNA was extracted with TRIzol (Life Technologies). Biotin-labeled cRNA was synthesized and hybridized to GeneChip U133 plus 2 (Affymetrix) according to the manufacturer's instruction. Gene expression data were normalized by using the MAS5 algorithm. Data were deposited in National Center for Biotechnology Information Gene Expression Omnibus (GEO) database (GEO accession no. GSE19678; www.ncbi.nlm.nih.gov/geo/).

**Immunoblotting.** An anti-DACH1 antibody was generated by immunization of GST-fused DACH1 protein and purified by affinity-purification with Immunogen-bound beads. Immunoblot was performed by using anti-DACH1 or anti–β-actin (AC-40; Sigma) antibody according to a previous report (49). Cell lysates at 3 d after the addition of doxycycline or RNAi treatment were used.

**Spheroid Formation Assay.** Expression of DACH1 was induced by exposure of U87TR-Da-clone16 or -clone18 cells to doxycycline for 72 h and then cells were grown in NBE medium (22, 50) composed of Neurobasal Medium (Life

Technologies), *N*-2, B-27 supplement (0.5× each; Life Technologies), human recombinant bFGF (50 ng/mL; PeproTech), and EGF (50 ng/mL; Life Technologies). At 10 d after medium change, the number of spheroid-forming colonies was counted. Paraformaldehyde-fixed spheroids were stained with an anti-Nestin monoclonal antibody (BD Biosciences) and Alexa488-conjugated anti-mouse IgG antibody (Life Technologies).

**In Vivo Studies.** Male 6- to 8-wk-old male athymic (nude) mice (nu/nu) of BALB/c were purchased from Charles River Laboratory Japan. For assessment of in vivo tumor growth, U87TR-Da cells were injected s.c. into the flank of mice. At the start point (day 0), drinking water was replaced with doxycycline-containing water for induction of DACH1 expression. For assessment of tumorigenicity, before injection, DACH1 expression was induced by the exposure of the U87TR-Da clone-16 cells with doxycycline for 10 d. The tumor formation was observed after s.c. injection of the serially diluted cells. For intracerebral stereotactic inoculation, cells in 6 μL of PBS were implanted into the right corpus striatum of the anesthetized mouse brain. Animal studies were performed according to institutional guidelines. See details of in vivo tumor growth and tumorigenicity assay in *SI Methods*.

Full methods and any associated references are available in *SI Methods*. Primers used were listed in Table S3.

**ACKNOWLEDGMENTS.** We thank Saori Kawanabe for technical assistance, Hiroko Meguro for GeneChip analysis, Kaoru Nakano for MassARRAY analysis, Dr. Junji Shibahara and Kotaro Onishi for immunohistochemistry, Drs. Aya Nonaka, Asuka Morizane, and Jun Takahashi for cell culture, and Drs. Vincent Stanton, Haruhiko Sugimura, Toru Niwa, Hiroaki Ikushima, Shogo Yamamoto, Takayuki Isagawa, and Genta Nagae for helpful comments. This work was supported by Grant-in-Aid for Young Scientists (B) 21790380 (to A.W.); and Grants-in-Aid for Scientific Research (S) 20221009 and Scientific Research on Priority Areas 17015008 from the Ministry of Education, Culture, Sports, Science and Technology-Japan, and Core Research for Evolutional Science and Technology from Japan Science and Technology (all to H.A.).

1. Furnari FB, et al. (2007) Malignant astrocytic glioma: Genetics, biology, and paths to treatment. *Genes Dev* 21:2683–2710.
2. Holland EC (2001) Gliomagenesis: Genetic alterations and mouse models. *Nat Rev Genet* 2:120–129.
3. Ohgaki H, Kleihues P (2007) Genetic pathways to primary and secondary glioblastoma. *Am J Pathol* 170:1445–1453.
4. Ishikawa S, et al. (2005) Allelic dosage analysis with genotyping microarrays. *Biochem Biophys Res Commun* 333:1309–1314.
5. Zhao X, et al. (2004) An integrated view of copy number and allelic alterations in the cancer genome using single nucleotide polymorphism arrays. *Cancer Res* 64:3060–3071.
6. Nannya Y, et al. (2005) A robust algorithm for copy number detection using high-density oligonucleotide single nucleotide polymorphism genotyping arrays. *Cancer Res* 65:6071–6079.
7. Midorikawa Y, et al. (2006) Molecular karyotyping of human hepatocellular carcinoma using single-nucleotide polymorphism arrays. *Oncogene* 25:5581–5590.
8. Gaasenbeek M, et al. (2006) Combined array-comparative genomic hybridization and single-nucleotide polymorphism-loss of heterozygosity analysis reveals complex changes and multiple forms of chromosomal instability in colorectal cancers. *Cancer Res* 66: 3471–3479.
9. Midorikawa Y, et al. (2009) Allelic imbalances and homozygous deletion on 8p23.2 for stepwise progression of hepatocarcinogenesis. *Hepatology* 49:513–522.
10. Cancer Genome Atlas Research Network (2008) Comprehensive genomic characterization defines human glioblastoma genes and core pathways. *Nature* 455:1061–1068.
11. Komura D, et al. (2006) Genome-wide detection of human copy number variations using high-density DNA oligonucleotide arrays. *Genome Res* 16:1575–1584.
12. Ueki K, et al. (1996) CDKN2/p16 or RB alterations occur in the majority of glioblastomas and are inversely correlated. *Cancer Res* 56:150–153.
13. Yin Y, Shen WH (2008) PTEN: A new guardian of the genome. *Oncogene* 27:5443–5453.
14. van Puijenbroek M, et al. (2005) Mass spectrometry-based loss of heterozygosity analysis of single-nucleotide polymorphism loci in paraffin embedded tumors using the MassEXTEND assay: Single-nucleotide polymorphism loss of heterozygosity analysis of the protein tyrosine phosphatase receptor type J in familial colorectal cancer. *J Mol Diagn* 7:623–630.
15. Tai AL, et al. (2006) High-throughput loss-of-heterozygosity study of chromosome 3p in lung cancer using single-nucleotide polymorphism markers. *Cancer Res* 66:4133–4138.
16. Miyazono K, Maeda S, Imamura T (2006) Smad transcriptional co-activators and co-repressors. *Smad Signal Transduction*, eds Dijke Pt, Heldin C-H (Springer, Dordrechet, The Netherlands), pp 277–293.
17. Wu K, et al. (2007) Cell fate determination factor DACH1 inhibits c-Jun-induced contact-independent growth. *Mol Biol Cell* 18:755–767.
18. Wu K, et al. (2006) DACH1 is a cell fate determination factor that inhibits cyclin D1 and breast tumor growth. *Mol Cell Biol* 26:7116–7129.
19. Ikushima H, et al. (2009) Autocrine TGF-beta signaling maintains tumorigenicity of glioma-initiating cells through Sry-related HMG-box factors. *Cell Stem Cell* 5:504–514.
20. Galli R, et al. (2004) Isolation and characterization of tumorigenic, stem-like neural precursors from human glioblastoma. *Cancer Res* 64:7011–7021.
21. Singh SK, et al. (2003) Identification of a cancer stem cell in human brain tumors. *Cancer Res* 63:5821–5828.
22. Lee J, et al. (2006) Tumor stem cells derived from glioblastomas cultured in bFGF and EGF more closely mirror the phenotype and genotype of primary tumors than do serum-cultured cell lines. *Cancer Cell* 9:391–403.
23. Takahashi JA, et al. (1992) Correlation of basic fibroblast growth factor expression levels with the degree of malignancy and vascularity in human gliomas. *J Neurosurg* 76:792–798.
24. Morrison RS, et al. (1994) Basic fibroblast growth factor and fibroblast growth factor receptor I are implicated in the growth of human astrocytomas. *J Neurooncol* 18:207–216.
25. Wong KK, et al. (2006) Genome-wide allelic imbalance analysis of pediatric gliomas by single nucleotide polymorphic allele array. *Cancer Res* 66:11172–11178.
26. Fan X, et al. (2002) Genetic profile, PTEN mutation and therapeutic role of PTEN in glioblastomas. *Int J Oncol* 21:1141–1150.
27. Parsons DW, et al. (2008) An integrated genomic analysis of human glioblastoma multiforme. *Science* 321:1807–1812.
28. Yan H, et al. (2009) IDH1 and IDH2 mutations in gliomas. *N Engl J Med* 360:765–773.
29. Watanabe T, Nobusawa S, Kleihues P, Ohgaki H (2009) IDH1 mutations are early events in the development of astrocytomas and oligodendrogliomas. *Am J Pathol* 174:1149–1153.
30. Zhao S, et al. (2009) Glioma-derived mutations in IDH1 dominantly inhibit IDH1 catalytic activity and induce HIF-1alpha. *Science* 324:261–265.
31. Biesiada E, Razandi M, Levin ER (1996) Egr-1 activates basic fibroblast growth factor transcription. Mechanistic implications for astrocyte proliferation. *J Biol Chem* 271: 18576–18581.
32. Xie TX, et al. (2006) Activation of stat3 in human melanoma promotes brain metastasis. *Cancer Res* 66:3188–3196.
33. Campanelli JT, et al. (2008) Expression profiling of human glial precursors. *BMC Dev Biol* 8:102.
34. Zhang SC, Wernig M, Duncan ID, Brüstle O, Thomson JA (2001) In vitro differentiation of transplantable neural precursors from human embryonic stem cells. *Nat Biotechnol* 19:1129–1133.
35. Noble M, Mayer-Pröschel M (1997) Growth factors, glia and gliomas. *J Neurooncol* 35: 193–209.
36. Peñuelas S, et al. (2009) TGF-beta increases glioma-initiating cell self-renewal through the induction of LIF in human glioblastoma. *Cancer Cell* 15:315–327.
37. Quiñones-Hinojosa A, Chaichana K (2007) The human subventricular zone: A source of new cells and a potential source of brain tumors. *Exp Neurol* 205:313–324.
38. Sanai N, Alvarez-Buylla A, Berger MS (2005) Neural stem cells and the origin of gliomas. *N Engl J Med* 353:811–822.
39. Li X, Perissi V, Liu F, Rose DW, Rosenfeld MG (2002) Tissue-specific regulation of retinal and pituitary precursor cell proliferation. *Science* 297:1180–1183.
40. Li X, et al. (2003) Eya protein phosphatase activity regulates Six1-Dach-Eya transcriptional effects in mammalian organogenesis. *Nature* 426:247–254.
41. Mardon G, Solomon NM, Rubin GM (1994) dachshund encodes a nuclear protein required for normal eye and leg development in Drosophila. *Development* 120: 3473–3486.
42. Shen W, Mardon G (1997) Ectopic eye development in Drosophila induced by directed dachshund expression. *Development* 124:45–52.
43. Lecuit T, Cohen SM (1997) Proximal-distal axis formation in the Drosophila leg. *Nature* 388:139–145.
44. Machon O, et al. (2002) Forebrain-specific promoter/enhancer D6 derived from the mouse Dach1 gene controls expression in neural stem cells. *Neuroscience* 112:951–966.
45. Heanue TA, et al. (2002) Dach1, a vertebrate homologue of Drosophila dachshund, is expressed in the developing eye and ear of both chick and mouse and is regulated independently of Pax and Eya genes. *Mech Dev* 111:75–87.
46. Jing Y, et al. (2011) In vitro differentiation of mouse embryonic stem cells into neurons of the dorsal forebrain. *Cell Mol Neurobiol* 31:715–721.
47. Wu K, et al. (2011) Cell fate determination factor Dachshund reprograms breast cancer stem cell function. *J Biol Chem* 286:2132–2142.
48. Louis DN, et al. (2007) The 2007 WHO classification of tumours of the central nervous system. *Acta Neuropathol* 114:97–109.
49. Watanabe A, et al. (2003) An opposing view on WWOX protein function as a tumor suppressor. *Cancer Res* 63:8629–8633.
50. Galli R, et al. (2002) Emx2 regulates the proliferation of stem cells of the adult mammalian central nervous system. *Development* 129:1633–1644.

Radiotherapy and Oncology 100 (2011) 380–385

Contents lists available at SciVerse ScienceDirect

Radiotherapy and Oncology

journal homepage: www.thegreenjournal.com

Cone beam CT

# 4D-CBCT reconstruction using MV portal imaging during volumetric modulated arc therapy

Satoshi Kida, Naoya Saotome, Yoshitaka Masutani, Hideomi Yamashita, Kuni Ohtomo, Keiichi Nakagawa, Akira Sakumi, Akihiro Haga *

*Department of Radiology, University of Tokyo Hospital, Japan*

ARTICLE INFO

*Article history:*
Received 23 July 2011
Received in revised form 29 August 2011
Accepted 30 August 2011
Available online 29 September 2011

*Keywords:*
CBCT
4D-CT
Respiratory motion
Portal imaging
VMAT

ABSTRACT

*Background:* Recording target motion during treatment is important for verifying the irradiated region. Recently, cone-beam computed tomography (CBCT) reconstruction from portal images acquired during volumetric modulated arc therapy (VMAT), known as VMAT-CBCT, has been investigated. In this study, we developed a four-dimensional (4D) version of the VMAT-CBCT.

*Materials and methods:* The MV portal images were sequentially acquired from an electronic portal imaging device. The flex, background, monitor unit, field size, and multi-leaf collimator masking corrections were considered during image reconstruction. A 4D VMAT-CBCT requires a respiratory signal during image acquisition. An image-based phase recognition (IBPR) method was performed using normalised cross correlation to extract a respiratory signal from the series of portal images.

*Results:* Our original IBPR method enabled us to reconstruct 4D VMAT-CBCT with no external devices. We confirmed that 4D VMAT-CBCT was feasible for two patients and in good agreement with in-treatment 4D kV-CBCT.

*Conclusion:* The visibility of the anatomy in 4D VMAT-CBCT reconstruction for lung cancer patients has the potential of using 4D VMAT-CBCT as a tool for verifying relative positions of tumour for each respiratory phase.



Radiotherapy is complex and verification of treatment is crucial. Although portal images acquired during treatment with an electronic portal imaging device (EPID) have been used as a planar image guidance tool and for geometrical quality assurance, the recent development of EPID dosimetry has provided in vivo dosimetry verification [1–3]. A Linac-mounted kV-CBCT is a powerful tool for verifying anatomical positions [4,5]. Accompanying rotational treatment such as volumetric modulated arc therapy (VMAT), in-treatment kV-CBCT images that reflect the patient's treatment position can be acquired just after the treatment [6–8]. The four-dimensional (4D) version known as 'in-treatment 4D kV-CBCT' verifies the positions of targets, such as lung tumours, with respiratory motion [9]. Acquiring CBCT images during treatment requires an orthogonal imager and a Linac-mounted kV source, and the isocentre displacement of the kV beam from the treatment beam must be carefully considered. More importantly, in-treatment kV-CBCT could expose the patient to additional radiation.

Recently, CBCT reconstruction with portal images during VMAT or VMAT-CBCT has been investigated [10]. The advantages of VMAT-CBCT are (1) no additional radiation exposure and (2) reduced hardware requirements, making the VMAT-CBCT a promising tool for verification of irradiated areas and/or in vivo dosimetry.

The 4D version of CBCT still presents a problem in acquiring respiratory signals for portal images. Generally, there are two methods to synchronously measure a respiratory signal with image acquisition. One method uses an image-based phase recognition (IBPR) technique [11–13]. The other uses an external respiratory monitoring system (e.g. AZ-733V by Anzai Medical Cooperation and real-time position management by Varian Medical System) [14]. This study tested the IBPR technique. For kV-CBCT, a technique of tracking small regions through the time series of projection images based on a maximum normalised cross correlation (NCC) was developed [9]. With this technique, parameters such as the size of the area were adjusted for application to portal images.

This paper reports on the feasibility of using 4D VMAT-CBCT as a treatment verification tool in two lung cancer patients receiving VMAT. Validity was assessed by comparing the tumour positions between 4D VMAT-CBCT images and in-treatment 4D kV-CBCT images simultaneously acquired during VMAT delivery. The 4D VMAT-CBCT images were also evaluated with phantom testing.

* Corresponding author. Address: Department of Radiology, The University of Tokyo Hospital, 7-3-1 Hongo, Bunkyo-ku, Tokyo 113-8655, Japan.
*E-mail address:* haga-haga@umin.ac.jp (A. Haga).

0167-8140/$ - see front matter © 2011 Elsevier Ireland Ltd. All rights reserved.
doi:10.1016/j.radonc.2011.08.047

## Methods and materials

### *Outlook of the 4D VMAT-CBCT reconstruction process*

4D VMAT-CBCT reconstruction is performed as follows: VMAT for lung cancer was delivered with an Elekta Synergy accelerator operating at 6 MV. During beam delivery, portal images were sequentially collected by EPID with an interval of 0.46 s using Elekta iViewGT software. The portal image consists of 1024 × 1024 pixels with a size of 0.25 mm at the isocentre. At maximum, 256 projection images per reconstruction were obtained. In order to connect the portal images with the corresponding gantry angles, we employed a log file via the Elekta software protocol, iCom, which records the gantry angle information during treatment. This was followed by matching the multi-leaf collimator (MLC) shapes derived from the portal images with those from iCom.

The acquired portal images can include the shift due to the geometric non-idealities in the rotation of the gantry system. The geometric non-idealities were measured in advance for gantry angle intervals of 5 degrees by analysing 10 cm × 10 cm radiation fields; this correction (flex correction) was performed for each portal image. The response of EPID was also regularised by considering the background (BG), linearity of monitor unit (MU), and field size (output factor) effects. MLC masking correction was performed according to Poludniowski et al. [10]. The MLC masking correction extrapolates the data truncated by the MLC field shape to mitigate artifacts otherwise induced by the filter operation of the CBCT reconstruction algorithm. A value in the masked region can be adjusted arbitrarily if we are interested only in visual images, not quantitative densities, within the patient. We defined the masking factor as a ratio of the maximum pixel value. In this study, we applied masking factors of 0.56 and 0.76 for patients 1 and 2, respectively.

Reconstruction of 4D VMAT CT requires a respiratory phase in the system. In this study, portal-image based phase recognition (P-IBPR) was employed using NCC (see below). The periodic selection of portal images of only one specific respiratory phase enables image reconstruction for that phase. Projection images were classified into 4 phases and the reconstructions were performed with a filtered back-projection (FBP) algorithm. The sequential process was performed off-line.

### *Portal-image based phase recognition (P-IBPR)*

The method proposed here employs NCC with limited areas between adjacent portal images. Several rectangular areas ($w \times h = 5 \times 100$ pixels) are placed sequentially within exposed fields on each frame of the portal images to account for tumour motion. While a rectangular area in the current frame is fixed, an area on the next frame is moved so that the NCC value of the two areas is maximised. Movement is limited to the cranio-caudal axis. The position of the rectangular area was set to the initial position with respect to each portal image (see Fig. 1). By performing

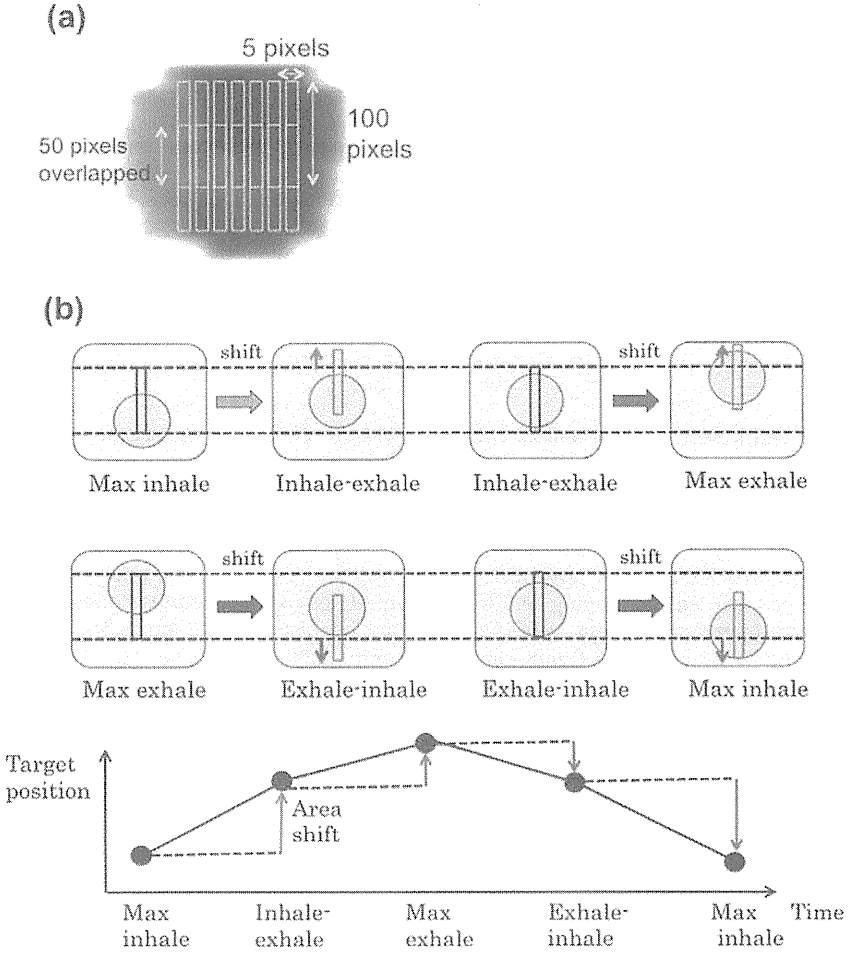


**Fig. 1.** (a) The distribution of several rectangular areas ($w \times h = 5 \times 100$ pixels) to cover tumour motion within exposed fields on each portal image. They are partially overlapped. (b) Schematic explanation of P-IBPR using NCC. The positions of the rectangular areas are shifted only along the cranio-caudal axis on the next portal image to find the maximum value of NCC with the calculation area on the previous portal image. The position of the rectangular area was set to the initial position with respect to each portal image. For the above example, the black rectangles indicate initial position and red rectangles indicate the position that gives the maximum NCC value with the corresponding black rectangles.

this procedure repeatedly for all portal images, a respiration signal can be obtained by displacement in the cranio-caudal direction. The signals were averaged among the calculation areas. Finally, low periodic components more than 5 s and high periodic components less than 1 s were removed in the frequency domain by using the band pass filter. The phase distributions were phase 0% (max inhale), phase 25% (inhale–exhale), phase 50% (max exhale), and phase 75% (exhale–inhale).

The efficiency of P-IBPR was determined by comparing the breathing pattern acquired by P-IBPR with those measured by visual tracking of the tumour on portal images. Here, the breathing cycle period was defined as the interval between adjacent max-expiration phases. In the visual tracking, a slight shaking can be recognised as a peak of expiration. Therefore, respirations with amplitudes less than 1 mm were neglected in the detection of max exhale.

*Treatment planning for VMAT*

One potential problem when inverse planning for lung cancer treatment is that the optimisation of beam fluences only takes into account a single three-dimensional volumetric data set. For this, the actual VMAT that continuously delivers the dose in all respiratory phases, may yield a dose distribution that differs from the plan. In order to compensate for this fact, the target volume can be extended to encompass the range of target motion by using 4D-CT scan, and field shapes can be defined as the target surroundings. Alternatively, the inverse plan that constrains MLC motion in VMAT forms field shapes that do not hide the target in lung cancer treatment. In this case, the beam intensity is mainly modulated by changing gantry speed and dose rate.

In this study, the planning target volume (PTV) for the lung tumour was created with a 5-mm margin of internal target volume generated from 20 4D-CT sets by using a 320-slice volumetric CT scanner (TOSHIBA, Japan). The patients received a D95 prescription of 50 Gy for PTV in 4 fractions. The single-arc VMAT with 6 MV was created by SmartArc in the Pinnacle v9.0 treatment planning system (Philips, USA). The constraint on MLC motion of 0.1 cm/degree was applied in the VMAT inverse plan so that MLC had little chance to hide the PTV. Such a constraint on MLC motion may significantly affect the quality of a treatment plan. Therefore, these plans were compared to those without constraints on MLC motion.

Treatment was performed by a single clockwise rotation (360 degrees). The arc used for reconstruction was from −180 to −19 degrees (patient 1) and from −180 to −40 degrees (patient 2). The angle range to allow portal imaging was limited by the Elekta iView software such that the maximum number of sequential acquisitions was 256. The difference between patients was due to the gantry speed determined by the VMAT plan.

Before applying the method to clinical cases, we conducted a 4D VMAT-CBCT reconstruction experiment by using the QUASAR respiratory motion phantom (Modus Medical Devices Inc.). The mechanical amplitude and cycle in the phantom were set at 10 mm and 3 s, respectively. The VMAT plan for patient 1 was delivered.

## Result

*VMAT plan with the MLC constraint*

The dose-volume histograms (DVHs) for patients 1 and 2 are shown in Fig. 2a and b, respectively. The solid curves denote the DVHs with an MLC constraint of 0.1 cm/degree, while the dashed curves denote DVHs without MLC constraints. The dose homogeneity of the plan without MLC constraint was better than the plan with MLC constraint for both patients. Dose conformity was

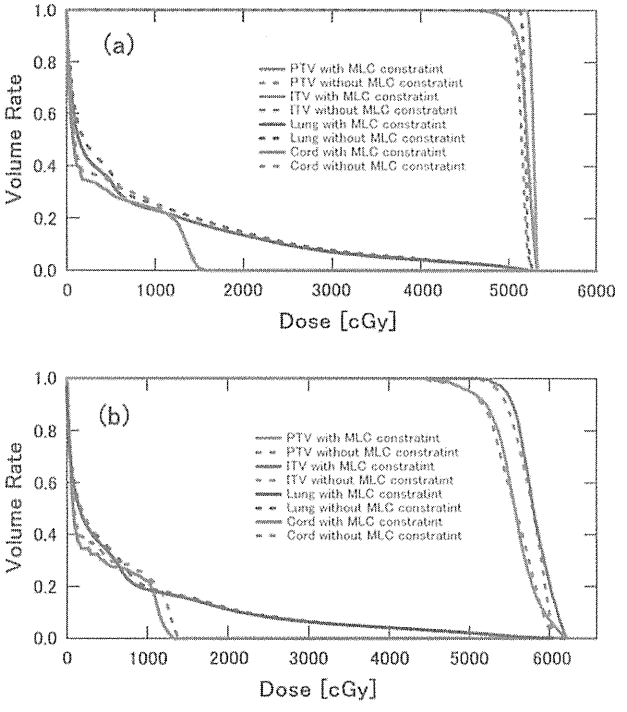


**Fig. 2.** DVH with and without MLC constraints for (a) patient 1 and (b) patient 2, All plans were prescribed as D95 of PTV equal to 50 Gy. The solid curves denote the DVHs with MLC constraint of 0.1 cm/degree, while the dashed curves denote those without MLC constraint.

comparable. On the other hand, the DVHs for organ at risk (OAR) with MLC constraint were slightly better than the DVHs without MLC constraint. This is presumably because in inverse planning, the constraint on homogeneity and conformity for PTV was stronger than the DVH constraint on OAR.

We found little difference between the plans with and without MLC constraints in the tested patients. The plans with MLC constraints were acceptable for clinical use and the MLC constraint was judged to manage the target motion without significant degradation of plan quality.

*Acquisition of respiratory signal*

The respiratory behaviours of two patients assessed by our P-IBPR method are shown in Fig. 3a and b. The original signal could have pseudo periodic components, such as those generated by gantry rotation. These components were removed by the band pass filter and, as seen in Fig. 3c and d, the motion due to patient respiration was clearly dissolved in all gantry angle directions. In Fig. 4, the breathing cycles were compared with those derived from the tumour motion in visual tracking. In Fig. 4a and b for patient 1, the breathing cycle was estimated by 3.7 ± 0.4 (1 SD) for both P-IBPR and visual tracking, while in Fig. 4c and d for patient 2, the breathing cycle was estimated by 2.7 ± 0.3 (1 SD) and 2.7 ± 0.4 (1 SD) for P-IBPR and visual tracking, respectively. The result in P-IBPR was concordant with the result of visual tracking. The difference of breathing cycle between P-IBPR and visual tracking was one sampling time (0.46 s) at most.

*Reconstruction of 4D VMAT-CBCT in phantom*

The reconstruction images of 4D VMAT-CBCT with an FBP algorithm corresponding to the points of maximum oscillation are shown in Fig. 5a and b. The standard calculation time for reconstruction with 270 × 270 × 80 voxels was about 10 s by GPU using

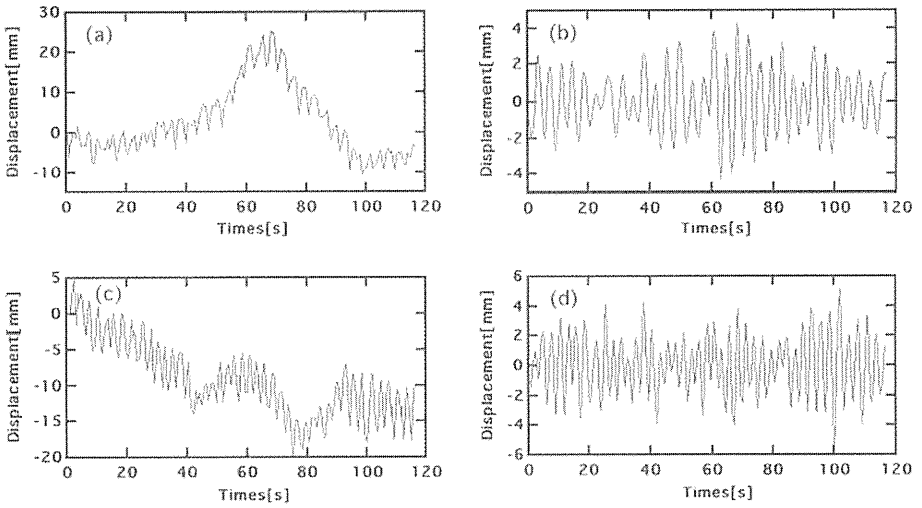


**Fig. 3.** Respiratory signal acquired by P-IBPR for patient 1 (a) before filtering and (b) after filtering and for patient 2 (c) before filtering and (d) after filtering.

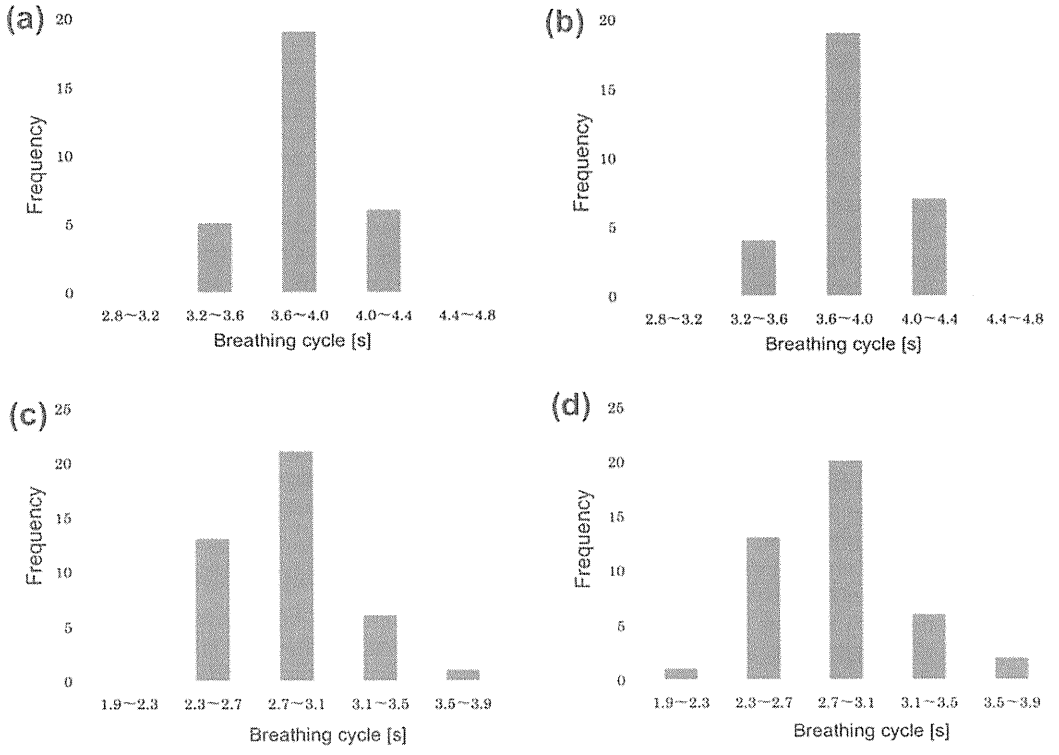


**Fig. 4.** Histograms of breathing cycle analysed by P-IBPR and visual tracking; (a) P-IBPR and (b) visual tracking for patient 1 and (c) P-IBPR and (d) visual tracking for patient 2.

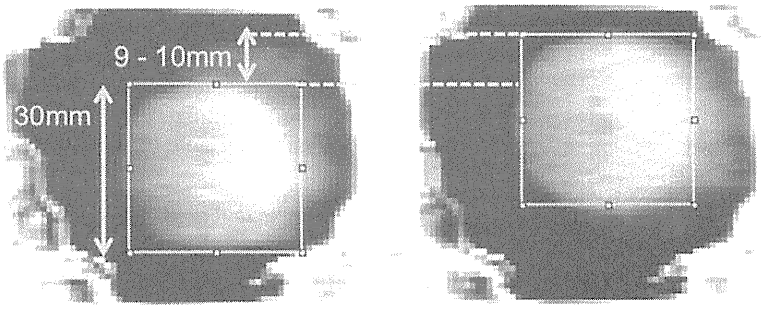


**Fig. 5.** Coronal images of 4D VMAT-CBCT of the QUASAR phantom in each peak. The diameter of the ball was 30 mm. The displacement was evaluated to be about 9–10 mm.

NAVIDIA Tesla C1060 4 GB. The amplitude was evaluated at about 9–10 mm from the 4D VMAT-CBCT images. This displacement is close to the mechanical set of 10 mm in the experiment. The inhomogeneous value inside the insert was observed.

*Reconstruction of 4D VMAT-CBCT in 2 patients*

With the respiratory signals acquired by P-IBPR, the portal images were classified into 4 phase bins. Then, VMAT-CBCT reconstruction was performed. For comparison, kV projection images were simultaneously acquired during VMAT, and 4D kV-CBCT was reconstructed. Fig. 6a and b illustrate the coronal and sagittal slices of VMAT-CBCT and kV-CBCT for 3D and the respiratory phases (max exhale, exhale inhale, max inhale, and inhale exhale) of patients 1 and 2.

The total number of portal images acquired during VMAT was 254 for both patients. Those images were almost equally classified into each phase bin. The gantry angle increment per projection for 4D reconstruction is dependent not only on the gantry speed but also on the respiratory cycle of the patient. These values for patients 1 and 2 were estimated as $5.4 \pm 0.8$ (1SD) and $3.9 \pm 0.5$ (1SD) degrees, respectively. Admittedly, there were large projection gaps that degraded image quality. In addition, this "effective" gantry angle increment included the error caused by the long acquisition interval of portal images, which was limited to 0.46 s per projection.

The centre of mass (COM) positions of the tumour during treatment were estimated from a contour of the tumour in respective max-exhale volume images in the Pinnacle treatment planning system and by shifting these contours in the other images. The shifts from the max exhale are denoted in Fig. 6. The results of 4D MV-CBCT were remarkably close to those of 4D kV-CBCT. The amplitudes of tumour motion during treatment for patients 1 and 2 were estimated to be about (1, 2, 5) and (2, 4, 5) mm, respectively. On the other hand, it was difficult to estimate tumour size due to diminished image quality and artifacts.

## Discussion

It should be noted that an exact and unique cone-beam reconstruction from portal images acquired in a VMAT delivery is impossible in principle [10]. That is, the VMAT-CBCT including our method is based on the assumption that there are few structures outside the radiation field. The effect of passing through objects outside the reconstructed region is naively considered by masking correction. However, as seen in Figs. 5 and 6 4D VMAT-CBCT showed the tumour position to be similar when predicted mechanically by the phantom and by the 4D kV-CBCT. We emphasise that we are interested in the visualisation of tumour motion for verification of actual treatment. From this viewpoint, we are satisfied that the amplitude can be evaluated from the 4D VMAT-CBCT images. Our method is, therefore, feasible for verifying tumour motion through the course of treatment. On the other hand, it should be noted that inconsistencies, such as the lack of projection data provided the degradation of image quality, and may lead to incorrect recognition for the tumour size and shape.

We employed the IBPR method using NCC to derive respiratory signals from portal images. Our experiments demonstrated that NCC can work well for frame-by-frame changes in irradiation intensity. Respiratory signals were readily obtained because the MLC speed was constrained by treatment planning optimisation. This constraint yielded field shapes similar to those created in conformal treatment. The fact that the tumour was located in the middle of the lung may explain why the MLC did not need to move drastically. Thus, a target was detected within a field through

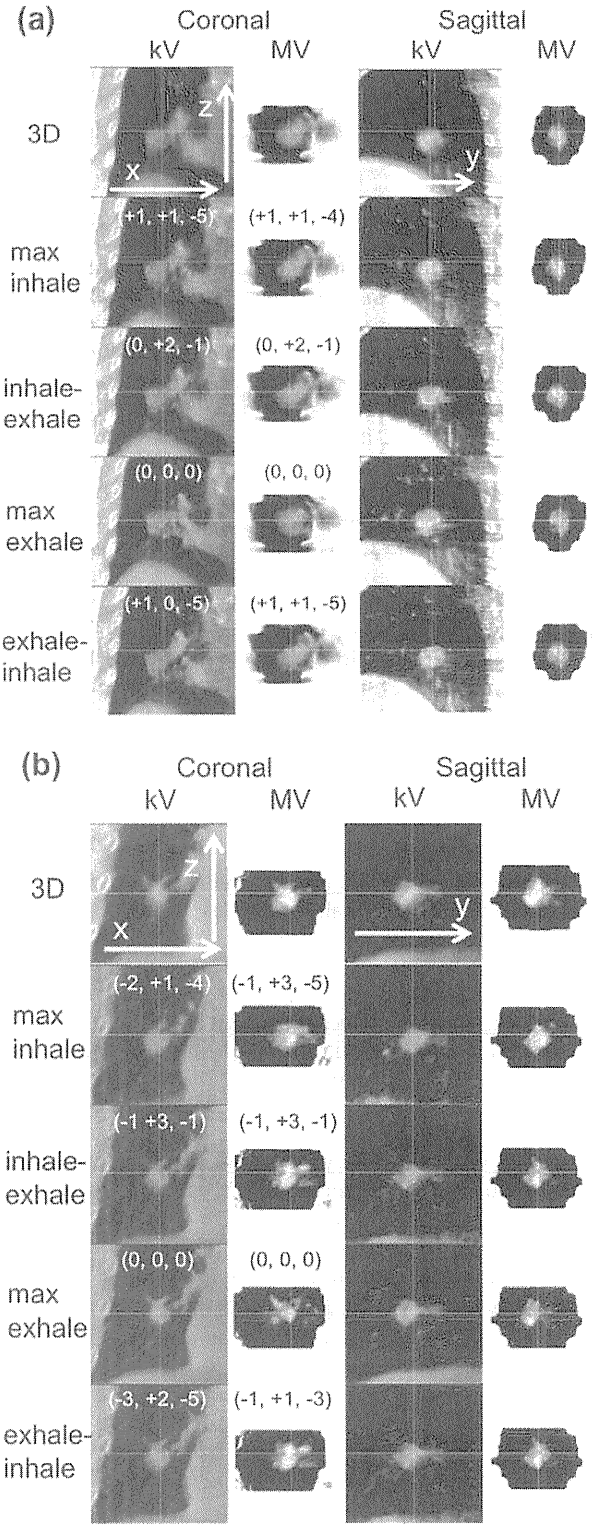


**Fig. 6.** Coronal and sagittal images at the isocentre plane of in-treatment kV 3D- and 4D-CBCT and 3D- and 4D-VMAT CT for (a) patient 1 and (b) patient 2. The coordinates inside the images represent the COM of tumour shift from max exhale with units in mm for each modality. The COMs were estimated from a contour delineated in respective max-exhale volume images on the Pinnacle treatment planning system and by shifting the contour in the other images.

almost all angles. On the other hand, the MLC constraint in the inverse plan may hinder clinical utility due to degradation of plan quality. In our clinical cases, this degradation was small and we judged that suppressing the MLC motion was beneficial for the